SAPIENZA
UNIVERSITÀ DI ROMA

Study of data analysis methods for the search of gravitational waves from primordial black hole binaries

Candidate

Elisa Velcani

ID number 1703044

Thesis Advisor

Dr. Cristiano Palomba

Thesis not yet defended

Study of data analysis methods for the search of gravitational waves from primordial black hole binaries
Master's thesis. Sapienza – University of Rome

This thesis has been typeset by LaTeX and the Sapthesis class.

Author's email: velcani.1703044@studenti.uniroma1.it

"Everyone knew it was impossible,
until a fool who didn't know came along and did it."
Albert Einstein

A papà,

a mamma,

a mio fratello.

Abstract

My thesis project aims to study a new data analysis method for the GW signal emitted binary systems made of sub-solar mass primordial black holes.

Considering a mass range of $[10^{-5}, 10^{-3}]M_\odot$, primordial black hole binaries in the inpiral phase are expected to emit continuous wave signals, which have a duration of the order of months to years.

In this thesis, I described a new data analysis procedure based on a semi-coherent hierarchical approach. The method is then applied to simulated signals injected into real data (run O3). In order to carry out these studies, I used pre-existing codes,developed for nearly monochromatic signals, that I generalised to the case of signals emitted by binary inspirals from specific locations, like the galactic center. In addition, I presented an estimate of the sensitivity of the proposed methodology. We have shown that with the heterodyne procedure we are able to perform a coarse initial correction and that the signal can be corrected perfectly after the implementation of a refined correction. Furthermore, we have proven that the galactic centre can be reached for a large portion of the considered parameter space.

Contents

Introduction

On 14th September 2015, the first gravitational wave was detected; this event marked the beginning of the gravitational wave era. It was a transient signal from a binary black-hole coalescence, recorded as GW150914. [4]

The discovery of gravitational waves is not only yet another experimental confirmation of the validity of Einstein's theory of General Relativity, but also opened a new window on the Universe and led to the birth of multi-messenger astrophysics.

The observation of gravitational waves (GW) from black hole (BH) mergers detected by the LIGO/Virgo collaboration during the three runs of observation (O1-O2-O3) has revived interest in understanding the origin of the merging BH population. A fascinating scenario is represented by Primordial Black Holes (PBHs). PBHs can form in the early Universe from the collapse of large density perturbations and might contribute to a fraction of the dark matter. A viable sub-class of PBH is represented by sub-solar mass BHs in binary systems. The detection of the GW emission from even a single source of this kind would unequivocally point to the primordial origin of the system components, as sub-solar mass BHs cannot be formed via stellar collapse. Due to their extremely small masses, sub-solar mass PBHs are expected to inspiral for very long times compared to typical LIGO/Virgo binary black hole signals, potentially for months or years. Therefore, PBH inspirals are ideal candidates for continuous- wave and transient continuous-wave searches. The confirmation of a primordial origin for any black hole would carry great implications, providing a unique window into early cosmology.

The thesis is structured as follows:

- In Chapter 1 the principles of gravitational wave theory are outlined and the solution of GWs is derived from Einstein's field equations in the linear approximation; after a brief introduction to GW source types, the focus is on gravitational signals emitted by binary systems of coalescing black holes and their expected waveform.

- In Chapter 2 some background information on the formation and characteristics of PBHs is discussed and estimates of the rates at which binary PBHs merge are provided to attend an event.

- In the first part of Chapter 3 I will prove that the GWs of sub-solar mass PBH binaries are well described by the quadrupole approximation during the inspiral phase, in order to reduce the parameter space. In the second part, we study the signal-to-noise ratio to demonstrate we can limit the analysis to the early inspiral phase, with a negligible loss of signal-to-noise ratio. This will

allow us to make more sensitive analysis keeping the computational cost under control.

- In Chapter 4 , which is the focus of my thesis, I will show a new data analysis method for the GW signal emitted by binaries of primordial black holes with sub-solar masses. The developed procedure is based on a hierarchical approach and has been tailored to search for continuous signals from specific sky locations, like Milky Way Galactic Center. I present results of validation tests, based on the application of the analysis pipeline to real data in which simulated signals have been injected. An estimation of the method sensitivity is also provided.

Chapter 1

Gravitational Waves

Gravitational Waves (*GWs*) have been first postulated by Albert Einstein in 1916 and their existence represents one of the most interesting predictions of the theory of General Relativity [25]. The first indirect proof of the existence of GWs is due to the work of Joseph Taylor and Russell Hulse (*Nobel Prize in 1993*). In 1974, they discovered the first binary pulsar system, called *PSR B1913+16*, composed by a pulsar and a neutron star. Subsequently, its orbital decay was observed. This matched exactly to the orbital decay predicted by General Relativity assuming the binary system was losing energy in the form of emitted GWs.

In Fig. (1.1) the prediction of General Relativity (solid curve) with respect to the acquired data (black points) is shown and the excellent agreement between observation and theory can be seen.
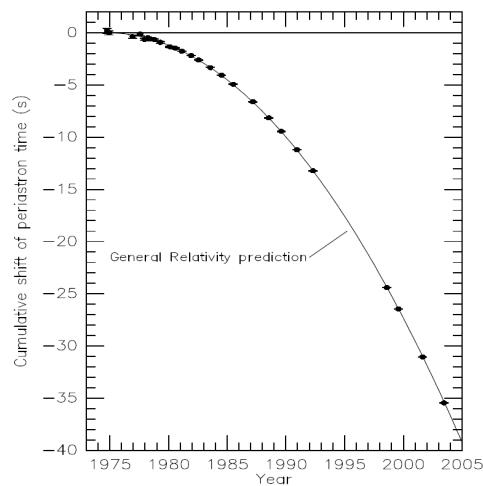

Figure 1.1. Orbital decay of PSR B1913+16 as a function of time. The points indicate the measurements of orbital phase shift for the passages to periastron. The curve represents the orbital phase shift expected from gravitational wave emission according to General Relativity. [47]

1.1 Theory of Gravitational Waves

In the last century, General Relativity has emerged as the best and strongest theory of gravity, due to the precise experimental tests of predicted phenomena that do not have Newtonian counterparts. The so-called "classical tests" were proposed by Einstein himself: the redshift of electromagnetic radiation, the precession of the perihelion of Mercury and the deflection of light rays. Two additional tests were later proposed, that is, the Shapiro delay and the Lense-Thirring dragging. [15]
The geometrical framework of General Relativity, which is a metric theory, is *spacetime*, which mathematically is represented by a four-dimensional differentiable manifold. The basic object that describes the spacetime geometry is the metric tensor $g_{\mu\nu}$. [33]
The fundamental relation of Einstein's theory is a tensor equation that describes gravity as a result of spacetime being curved by mass-energy, known as **Einstein's field equations**:

$$R_{\mu\nu} - \frac{1}{2}g_{\mu\nu}R = \frac{8\pi G}{c^4}T_{\mu\nu} \tag{1.1}$$

with $\mu, \nu = 0, 1, 2, 3$ [1]. Defining the *Einstein's tensor* as

$$G_{\mu\nu} = R_{\mu\nu} - \frac{1}{2}g_{\mu\nu}R$$

the Eq. (1.1) can be written as

$$G_{\mu\nu} = \frac{8\pi G}{c^4}T_{\mu\nu} \tag{1.2}$$

where $R_{\mu\nu}$ is the Ricci tensor, R the scalar curvature, $g_{\mu\nu}$ is the metric tensor and $T_{\mu\nu}$ the stress-energy tensor.

In order to get an insight to the meaning of these terms, we have to introduce those mathematical concepts that are necessary to correctly formulate the physical theory.[2]
The **metric tensor $g_{\mu\nu}$** has a central role in this theory: it is a rank-two, symmetric tensor and has ten independent components; it is called *metric* tensor because it allows to perform metric operations on a manifold.

To understand the left side of the Eq. (1.1), we have to introduce the affine connections, or *Christoffel symbols*. Let's consider a vector field $\vec{V} = V^\mu \vec{e}_{(\mu)}$, the derivative of the basis vector $\vec{e}_{(\mu)}$ is

$$\frac{\partial \vec{e}_{(\alpha)}}{\partial x^\beta} = \Gamma^\mu_{\alpha\beta}\vec{e}_{(\mu)}$$

where α indicates which basis vector $\vec{e}(\alpha)$ which we are differentiating while β

---

[1]Greek indices $(\mu, \nu, ..)$ denote the coordinate numbers from 0 to 3, while Roman indices $(i, j, .$ on) denote the coordinate numbers from 1 to 3.

[2]We recall that all formulas are written by applying Einstein's convention for the sum, i.e. a sum over repeated indices is left implicit.

indicates the coordinate with respect to which the differentiation is performed. We will denote the components of a partial derivative of a quantity f as $\partial f \equiv f_{,u}$. The term "$\Gamma^{\mu}_{\alpha\beta}$" indicates the *Christoffel symbols* and it represents the variation of the vectors due to the spacetime curvature. Christoffel's symbols are related to the metric components by the following relation:

$$\Gamma^{\sigma}_{\alpha\beta} = \frac{1}{2}g^{\sigma\mu}(g_{\mu\alpha,\beta} + g_{\mu\beta,\alpha} - g_{\alpha\beta,\mu}) \tag{1.3}$$

The **Ricci tensor, $R_{\mu\nu}$**, is a rank-2 tensor obtained by contraction of the Riemann tensor $R_{\alpha\beta\mu\nu}$[3] with the metric, i.e. $R_{\mu\nu} = g^{\alpha\beta}R_{\alpha\mu\beta\nu}$. The Riemann tensor depends on the affine connection and on its first derivatives, i.e. on the first and second derivatives of the metric tensor, according to the relation

$$R^{\alpha}_{\ \mu\beta\nu} = \Gamma^{\alpha}_{\beta\nu,\mu} - \Gamma^{\alpha}_{\beta\mu,\nu} - \Gamma^{\alpha}_{\sigma\nu}\Gamma^{\sigma}_{\beta\mu} - \Gamma^{\alpha}_{\sigma\mu}\Gamma^{\sigma}_{\beta\nu} \tag{1.4}$$

and it is a measure of the spacetime curvature: when it vanishes the corresponding spacetime is flat, instead, if the spacetime is curved the Rieamann tensor is not null; since it is a tensor, this is true in any coordinate frame. For this reason, it is also called *curvature tensor*.

The element R is the **scalar curvature** (or Ricci curvature): it is derived from Ricci tensor by further contracting the two indexes: $R = g^{\mu\nu}R_{\mu\nu}$.. As the Riemann tensor, both the Ricci tensor and the Ricci scalar are linear in the second derivatives of $g_{\mu\nu}$ and non-linear in the first derivatives.

Both in Special Relativity and General Relativity, the distribution of matter and energy can be described in terms of a symmetric rank-two tensor field, called the **stress-energy tensor $T_{\mu\nu}$**, which appear in the right side of Eq. (1.1).

We shall introduce first $T_{\mu\nu}$ in a flat spacetime. For this purpose, let us consider the simple case of a system of M non-interacting particles, each of which follows the worldline $\xi^{\alpha}_{n}(t)$ ($n = 0, 1..., M$) with the energy-momentum four-vector $p^{\alpha}_{n} = (p^{0}_{n}, p^{i}_{n})$ [4]. The stress-energy tensor is defined as

$$T^{\alpha\beta} = c^2 \sum_{n} p^{\alpha}_{n} \frac{d\xi^{\beta}_{n}}{dt} \delta^3(\boldsymbol{\xi} - \boldsymbol{\xi}_n(t)) \tag{1.5}$$

where with **bold** we indicate three-dimensional vectors. The function $\delta^3(\boldsymbol{\xi} - \boldsymbol{\xi}_n(t))$ is the three-dimensional Dirac δ-function.

In a flat spacetime, the components of the stress-energy tensor have a direct physical meaning.

- T^{00} has the dimensions of an energy divided by a volume, that is, the **Energy density** of the system, defined as

$$T^{00} \equiv \sum_{n} cp^{0}_{n}(t)\delta^3(\boldsymbol{\xi} - \boldsymbol{\xi}_n(t)) = \sum_{n} E_n \delta^3(\boldsymbol{\xi} - \boldsymbol{\xi}_n(t))$$

---

[3] $R_{\alpha\beta\mu\nu} = g_{\alpha\lambda}R^{\lambda}_{\beta\mu\nu}$

[4] The time component is $p^0 = mc\gamma = \frac{E}{c}$, where E is the particle energy, the space components are $p^i = m\gamma v^i$ and $\gamma = 1/\sqrt{1 - \frac{v^2}{c^2}}$

- $\frac{1}{c}T^{0i}$ is the **Density of momentum**, where T^{0i} is defined as

$$T^{0i} \equiv \sum_n c p_n^i(t)\delta^3(\boldsymbol{\xi} - \boldsymbol{\xi}_n(t))$$

and it can be interpreted as the energy flux per unit time across the unit surface orthogonal to axis ξ_i.

- T^{ki} is the **Momentum current**

$$T^{ki} \equiv \sum_n p_n^k(t)\frac{d\xi_n^i}{dt}\delta^3(\boldsymbol{\xi} - \boldsymbol{\xi}_n(t))$$

and this represents the flux of the *k-th* component of the momentum per unit time across the unit surface orthogonal to the axis ξ_i.

An alternative way of writing Eq. (1.5) is

$$T^{\alpha\beta} = c\sum_n \int p_n^\alpha \frac{d\xi_n^\beta}{d\tau_n}\delta^4(\vec{\xi} - \vec{\xi}_n(\tau_n))d\tau_n \tag{1.6}$$

where the " $\rightarrow$ " stands for a four-dimensional vector.
This equation can be generalized to the case of curved spacetime as

$$T^{\alpha\beta} = c\sum_n \int \frac{1}{\sqrt{-g}}p_n^\alpha \frac{dx_n^\beta}{d\tau_n}\delta^4(\vec{x} - \vec{x}_n(\tau_n))d\tau_n \tag{1.7}$$

where the term $\frac{1}{\sqrt{-g}}$ derives from the transformation of the delta-function $\delta^4(\vec{\xi}-\vec{\xi}_n) = \frac{\delta^4(\vec{\xi}-\vec{\xi}_n)}{\sqrt{-g}}$ and g stands for the determinant of the metric tensor. Eq. (1.7) is a generic expression that is valid both in flat and in curved spacetime.[5]

In Special Relativity, i.e. in the absence of gravity, the stress-energy tensor allows us to express conservation of energy-momentum as

$$T^{\alpha\beta}{}_{,\beta} = 0. \tag{1.8}$$

However, this conservation law cannot be extended to General Relativity. Indeed, the generalization of (1.8) in curved spacetime is

$$T^{\alpha\beta}{}_{;\beta} = 0 \tag{1.9}$$

and it is possible to demonstrate that this equation does not lead to conserved quantities. [26]
For instance, for a perfect fluid the energy-momentum tensor reads

$$T^{\alpha\beta} = (\epsilon + p)u^\alpha u^\beta + pg^{\alpha\beta}$$

where u^α is four-velocity field, ϵ and P are respectively the energy density and the pressure of the fluid measured in a LICF system (*Locally inertial comoving frame).*

Finally, it's important to note that the term $\frac{8\pi G}{c^4} \sim 10^{-50}s^2/g \cdot cm$ is very small and this is the reason why GWs are extremely weak and it is very difficult to detect them.

---

[5]For a flat spacetime $\sqrt{-g} = 1$ in Minkowskian coordinates and in a locally inertial frame (LIF).

As mentioned above, the existence of GWs is one of the central predictions of the theory of General Relativity. According to Einstein, when a mass-energy distribution varies over time, the information about gravitational field changes propagates with finite speed, the speed of light c, in the form of waves: these are GWs.

We shall study GWs with a "*perturbative approach*", which means that we consider the gravitational waves emitted by a source as small perturbations of a background solution. This approach does not require a particular symmetry of the spacetime, unlike the "*exact approach*". Indeed, in the exact approach we look for analytical solutions of the Einstein equation and this is possible only in the case of particular symmetries of the problem, such as the Schwarzschild solution. On the other hand, the perturbative approach requires the knowledge of the background solution. Finally, there is the *numerical approach* which consists of numerical integration of the full, non-linear Einstein equations. It is followed to solve problems that do not admit symmetries of spacetime or when the metric cannot be considered as a small perturbation of a background solution.

Let's focus now on the perturbative approach. We can write the metric tensor of the perturbed spacetime, $g_{\mu\nu}$, as:

$$g_{\mu\nu} = g^0_{\mu\nu} + h_{\mu\nu} \tag{1.10}$$

where $g^0_{\mu\nu}$ is the known solution of Einstein's equations, i.e. the background, and $h_{\mu\nu}$ is the small perturbation such as to satisfy the condition

$$|h_{\mu\nu}| \ll |g^0_{\mu\nu}|$$

Note that the stress-energy $T_{\mu\nu}$ is now:

$$T_{\mu\nu} = T^0_{\mu\nu} + \delta T_{\mu\nu}$$

where $T^0_{\mu\nu}$ describes the source that generates the background geometry while $\delta T_{\mu\nu}$ is associated to the source that causes the small perturbation.

Far away from compact objects (black holes and neutrons stars), gravitation is "weak" in the sense that the spacetime geometry is nearly flat. Therefore, in most astrophysical situations, the physical metric is "close" to the Minkowski metric of special relativity [34], and the metric (1.10) can be written as

$$g_{\mu\nu} = \eta_{\mu\nu} + h_{\mu\nu} \tag{1.11}$$

where $\eta_{\mu\nu} = diag(-1, 1, 1, 1)$ is the Minkowsky metric tensor. This approximation is called *weak-field limit*. We work to linear order in $h_{\mu\nu}$ and we neglect all terms $O(h^2)$.

By inserting the perturbed metric tensor in the definitions of affine connection and Ricci tensor and performing all the calculation limiting the expansion to the first order in h, the solution is [26]:

$$\Box_F h_{\mu\nu} - \left[\frac{\partial^2}{\partial x^\lambda \partial x\mu} h^\lambda_\nu + \frac{\partial^2}{\partial x^\lambda \partial x\nu} h^\lambda_\mu - \frac{\partial^2}{\partial x^\mu \partial x\nu} h^\lambda_\lambda \right] = -\frac{16\pi G}{c^4} \left(\delta T_{\mu\nu} - \frac{1}{2} \eta_{\mu\nu} \delta T \right) \tag{1.12}$$

where $\Box_F = (-\frac{1}{c^2}\frac{\partial^2}{\partial t^2} + \nabla^2)$ is the d'Alambertian in flat spacetime.

This equation can be simplified by choosing a coordinate system in which the *harmonic gauge* condition

$$g^{\mu\nu}\Gamma^{\lambda}_{\mu\nu} = 0 \tag{1.13}$$

is satified. This leads to

$$\frac{\partial}{\partial x^{\mu}}h^{\mu}_{\nu} = \frac{1}{2}\frac{\partial}{\partial x^{\nu}}h^{\mu}_{\mu} \tag{1.14}$$

where $h = \eta^{\mu\nu}h_{\mu\nu} \equiv h^{\nu}_{\nu}$. Using this condition the terms in square brackets in Eq. (1.12) vanish and the Einstein equation with the condition (1.14) reduce to

$$\begin{cases} \Box_F h_{\mu\nu} = -\dfrac{16\pi G}{c^4}\left(\delta T_{\mu\nu} - \dfrac{1}{2}\eta_{\mu\nu}\delta T\right) \\ \dfrac{\partial}{\partial x^{\mu}}h^{\mu}_{\nu} = \dfrac{1}{2}\dfrac{\partial}{\partial x^{\nu}}h^{\mu}_{\mu} \end{cases} \tag{1.15}$$

It is useful to introduce the tensor

$$\bar{h}_{\mu\nu} \equiv h_{\mu\nu} - \frac{1}{2}\eta_{\mu\nu}h$$

and Eqs. (1.15) become

$$\begin{cases} \Box_F \bar{h}_{\mu\nu} = -\dfrac{16\pi G}{c^4}\delta T_{\mu\nu} \\ \dfrac{\partial}{\partial x^{\mu}}\bar{h}^{\mu}_{\nu} = 0 \end{cases} \tag{1.16}$$

Outside the source, where $\delta T_{\mu\nu} = 0$

$$\begin{cases} \Box_F \bar{h}_{\mu\nu} = 0 \\ \dfrac{\partial}{\partial x^{\mu}}\bar{h}^{\mu}_{\nu} = 0 \end{cases} \tag{1.17}$$

Note that Eq.(1.17) is just the D'Alambert equation for the metric perturbation $h_{\mu\nu}$ and it shows that a perturbation of a flat spacetime propagates as a wave travelling at the speed of light.

It should be stressed that if the harmonic gauge condition is not satisfied in the considered reference frame, we can perform an infinitesimal transformation of coordinates

$$x'^{\mu} = x^{\mu} + \epsilon^{\mu}(x)$$

where ϵ^{μ} is an arbitrary vector such that $\frac{\partial\epsilon^{\mu}}{\partial x'^{\mu}}$ is of the same order of $h_{\mu\nu}$; if ϵ^{μ} satisfies the following equation

$$\Box_F\epsilon_{\rho} = \frac{\partial h^{\beta}\rho}{\partial x^{\beta}} - \frac{1}{2}\frac{\partial h}{\partial x^{\rho}} \tag{1.18}$$

in the new reference frame of coordinates x'^{μ} the gauge condition is satisfied.

Notice that the harmonic gauge condition (1.14) does not uniquely specify the metric perturbation. Indeed, any gauge transformation such that ϵ^{μ} satisfies the equation $\Box_F\epsilon^{\mu} = 0$, does preserve the gauge condition.

In order to study the physical degrees of freedom we have to move to the *transverse-traceless gauge (TT-gauge)*. Let's perform the infinitesimal coordinate transformation written above in order that in the new frame the harmonic gauge condition is satisfied. We can choose the four functions ϵ^μ ($\mu = 0, 1, 2, 3$) to set to zero four quantities; for example, for a gravitational wave propagating along the x-direction, we can take

$$\bar{h}^t_x = \bar{h}^t_y = \bar{h}^t_z = \bar{h}^y_y + \bar{h}^z_z = 0 \tag{1.19}$$

From the gauge condition it follows that

$$\bar{h}^t_t = \bar{h}^x_t \qquad\qquad \bar{h}^t_y = \bar{h}^x_y$$
$$\bar{h}^t_x = \bar{h}^x_x \qquad\qquad \bar{h}^t_z = \bar{h}^x_z$$

and, given Eq.(1.19), it is also

$$\bar{h}^x_x = \bar{h}^x_y = \bar{h}^x_z = \bar{h}^t_t = 0 \tag{1.20}$$

The remaining *non-vanishing* components are $\bar{h}^z_y$ and $\bar{h}^y_y - \bar{h}^z_z$. Moreover, from Eqs. (1.19) and (1.20) it follows that:

$$\bar{h} = \bar{h}^\mu_\mu = 0$$

and since $\bar{h} = -h$, it follows that $h = 0$. Given that $h_{\mu\nu}$ and $\bar{h}_{\mu\nu}$ only differs for the *trace h*, they are the same in the *TT gauge*. Thus, with this gauge choice, the perturbation $h_{\mu\nu}$ can be written as:

$$h_{\mu\nu} = \begin{pmatrix} 0 & 0 & 0 & 0 \\ 0 & 0 & 0 & 0 \\ 0 & 0 & h_{yy} & h_{yz} \\ 0 & 0 & h_{yz} & -h_{yy} \end{pmatrix}$$

In conclusion, there are two physical degree of freedom which corresponds to the two polarization states; from now on, the perturbation with two identical index (h_{xx}, h_{yy}, h_{zz}) will be called h_+ while with mixed index such as $h_{xy}, h_{yz}, ...$, it will be $h_\times$:

$$h_{\mu\nu} = \begin{pmatrix} 0 & 0 & 0 & 0 \\ 0 & 0 & 0 & 0 \\ 0 & 0 & h_+ & h_\times \\ 0 & 0 & h_\times & -h_+ \end{pmatrix}$$

To give a representation of these polarization states we consider a sinusoidal GW propagating through a x-axis and a ring of particles centered at the origin in the (y,z) plane. The physical effect of both GW polarization h_+ and $h_\times$ can be observed in Fig. 1.2. Therefore, we can understand that the effect of a GW between two freely gravitating particles is to stretch and shrink the separation distance between them. The displacement ΔL between the particles will be: $\Delta L \sim hL$, where h is the GW strain. Thus, h is defined as the fractional change in length between two test masses:
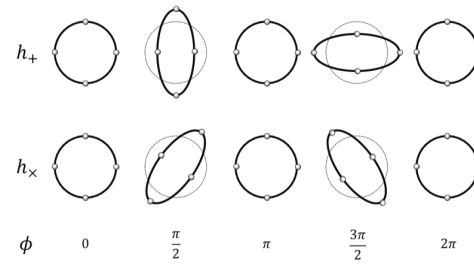
$$h \equiv \frac{\Delta L}{L} \tag{1.21}$$

Figure 1.2. The effect of the $+$ and x polarizations on a ring of particles. [11]

1.1.1   Quadrupole Approximation

In this section we will consider GWs emitted by dynamical systems described by a stress-energy tensor $T_{\mu\nu}$ on the assumption of **quadrupole approximation**. This assumption requires that the gravitational field is weak. We saw that in this limit, Einstein's equation reduce to eqs (1.16). In addition, the *slow-motion approximation* is assumed; this requires that the region with radius ϵ in which the source of GWs is confined is much smaller than the wavelength of the emitted radiation, $\lambda_{GW} = \frac{2\pi c}{\omega}$. This implies

$$\frac{2\pi c}{\omega} \gg \epsilon \qquad \rightarrow \qquad \epsilon\omega \ll c \qquad \rightarrow \qquad v_{source} \ll c \qquad (1.22)$$

Applying this condition, after several calculation we end up to a solution [26], written in terms of *retarded potentials*:

$$\bar{h}_{\mu\nu}(t,r) = \frac{4G}{c^4}\frac{1}{r}\int_V T_{\mu\nu}(t - \frac{r}{c}, x^{'})d^3x \qquad (1.23)$$

where V is the three-dimensional source volume. An observer located at the distance r from the source, at the time t receives a wave $\bar{h}_{\mu\nu}(t,r)$ which is the sum of the contributions emitted from each source element located in x' from the origin of a frame centered in some point within the source, at the retarded time $t' = t - \frac{r}{c}$. Let's introduce the *quadrupole moment tensor* defined as

$$q^{ik}(t) = \frac{1}{c^2}\int_V T^{00}(t,x)x^n d^3x \qquad (1.24)$$

and the *Tensor Virial Theorem* which states

$$\frac{1}{c^2}\frac{\partial^2}{\partial t^2}\int_V T^{00}x^i x^k d^3x = 2\int_V T^{ik}d^3x \qquad (1.25)$$

we can express the component of the perturbation in terms of quadrupole moment, obtaining the so-called **quadrupole formula**:

$$\begin{cases} \bar{h}^{\mu 0} = 0 & \mu = 0,...,3 \\ \bar{h}^{ik}(t,r) = \frac{2G}{c^4 r}\cdot[\frac{d^2}{dt^2}q^{ik}(t - \frac{r}{c})] \end{cases} \qquad (1.26)$$

where $\mu = 0,..,3$ and $i,k = 1,2,3$. Eqs. (1.26) represents the solution of Einstein's field equations in quadrupole approximation. This is a key result because shows that gravitational waves are generated by any time-varying quadrupole moment. In electromagnetism, while the electric charge (the monopole) is conserved, the electric dipole moment is not, so electromagnetic radiation is predominantly dipolar. Conversely, GWs do not have a dipolar contribution.

To project the wave in the TT-gauge we use the *transverse-traceless operator* which "extracts" the transverse-traceless part of a rank-two tensor on the three-dimensional Euclidean space:

$$\mathcal{P}_{jkmn} \equiv P_{jm}P_{kn} - \frac{1}{2}P_{jk}P_{mn}$$

where

$$P_{jk} \equiv \delta_{jk} - n_j n_k$$

By applying the projector $\mathcal{P}_{jkmn}$ either to h_{jk} or to $\bar{h}_{jk}$ (their differ only by the trace but $\mathcal{P}_{jkmn}$ extracs the traceless part of the tensor) we obtain the components of the metric perturbation in the TT gauge:

$$h_{jk}^{\mathbf{TT}} = \mathcal{P}_{jkmn} h_{mn} = \mathcal{P}_{jkmn} \bar{h}_{mn}$$

So, we can write the equations 1.26 in the TT gauge:

$$\begin{cases} h_{\mu 0}^{\mathbf{TT}} = 0 & \mu = 0, ..., 3 \\ h_{ik}^{\mathbf{TT}}(t,r) = \frac{2G}{c^4 r} \cdot [\frac{d^2}{dt^2} Q_{ik}^{\mathbf{TT}}(t - \frac{r}{c})] \end{cases} \quad (1.27)$$

where $Q_{jk}^{\mathbf{TT}} \equiv \mathcal{P}_{jkmn} q_{mn}$ is the *transverse-traceless part of the quadrupole moment.*

The emission of a GW implies a loss of energy by the system. In order to estimate the energy and momentum carried by the GW we introduce the stress-energy pseudo-tensor $t_{\mu\nu}$, which behaves likes a tensor only under linear coordinate transformations. We don't report here the explicit form of the pseudo-tensor but we say that its expression is quadratic in the Christoffel symbols, that are tensor only under linear coordinate transformations, and depends on the inverse metric tensor $g^{\mu\nu}$.
In general, the energy flowing across a unit surface orthogonal to the direction x' per unit time is given by (c times) the component $0x'$ of the stress-energy tensor. Similarly, the energy flux of a gravitational wave propagating in the direction "x'" is given by the component "0x'" of the stress-energy pseudo-tensor averaged over several wavelengths:

$$\frac{dE_{GW}}{dtdS} = < ct^{0x'} > \quad (1.28)$$

Given an observer who detects a wave emitted from a source propagating in a generic direction r with both the polarization h_+ e h_x, the expression of t^{0r} is: the expression of t^{0r} is:

$$t^{0r} = \frac{dE_{GW}}{dtdS} = \frac{c^3}{16\pi G} \left[\left(\frac{dh_+^{\mathbf{TT}}(t,r)}{dt} \right)^2 + \left(\frac{dh_\times^{\mathbf{TT}}(t,r)}{dt} \right)^2 \right]$$
$$= \frac{c^3}{32\pi G} \left[\sum_{ik} \left(\frac{dh_{ik}^{\mathbf{TT}}(t,r)}{dt} \right)^2 \right] \quad (1.29)$$

Substituting the expression h_{ij} given from eq. (1.27) and integrating respect to $dS = r^2 d\omega$, we find the gravitational luminosity, i.e. the energy carried by a GW per unit time:

$$L_{GW} = \int \frac{dE_{GW}}{dtdS} dS$$
$$= \frac{G}{2c^5} \frac{1}{4\pi} \int d\Omega < \sum_{jk} \left(\mathcal{P}_{jkmn} \dddot{Q}_{mn}(t - \frac{r}{c}) \right)^2 > \quad (1.30)$$
$$= \frac{G}{5c^5} < \sum_{k,n=1}^{3} \dddot{Q}_{kn}(t - \frac{r}{c}) \dddot{Q}_{kn}(t - \frac{r}{c}) >$$

Thus is an important result and we refer to Eq. (1.30) as **luminosity quadrupole formula**.

1.1.2   Post-Newtonian Formalism

The waveform derived through the quadrupole formalism corresponds to the lowest order term in a Post-Newtonian expansion of the equation of motion in the parameter

$$\epsilon \sim \sqrt{\frac{GM}{c^2 R}} \sim v/c$$

where v is the typical velocity of the source.

For a generic metric theory, Post-Newtonian formalism is an approximation to GR valid in the slow-motion and weak-field limit. It include the contributions of higher order multipole expansion of the metric $g_{\mu\nu}$ and stress-energy tensor $T^{\mu\nu}$.

Indicating with $^{(n)}g_{\mu\nu}$ the terms of order ϵ^n, the expansion of the metric is:

$$g_{00} = -1 + {}^{(2)}g_{00} + {}^{(4)}g_{00} + {}^{(6)}g_{00} + ...,$$

$$g_{0i} = {}^{(3)}g_{0i} + {}^{(5)}g_{0i} + ...,$$

$$g_{ij} = \delta_{ij} + {}^{(2)}g_{ij} + {}^{(4)}g_{ij} + ...,$$

The stress-energy tensor is expanded as

$$T^{00} = {}^{(0)}T^{00} + {}^{(2)}T^{00} + ..,$$

$$T^{0i} = {}^{(1)}T^{0i} + {}^{(3)}T^{0i} + ..,$$

$$T^{ij} = {}^{(2)}T^{ij} + {}^{(4)}T^{ij} + ..,$$

1.2 Sources of gravitational waves

GWs have been classified into four categories according to the nature of the source that generates them. Each different class generates characteristic set of signal and requires different approaches to the data-analysis problem.

Compact binary coalescence (CBC) GWs emitted by compact binary systems:
-Binary Neutron Star (BNS);
-Binary Black Hole (BBH);
-Neutron Star-Black Hole Binary (NSBH)
Since a binary system that radiates GWs and loses energy, the two constituents spiral closer and closer: as the separation decreases, the amplitude of the gravitational wave increases, leading to a characteristic "chirp" signal.

Periodic sources Rotating neutron stars (e.g. pulsars) isolated or in a binary system emit periodic gravitational wave signals if asymmetric with respect to their rotation axis.

Burst GWs generated by events such as Supernova explosions and the collapse of a star into neutron star or a black hole. The frequency of the radiated GW signal is less than a few kHz.

Stochastic sources A cosmological stochastic background of GWs is expected to have been generated during the phase transitions in the early universe and the inflationary phase. An astrophysical background is expected from the superposition of the GW signals due to the population of binary black hole and neutron star.

1.3 Gravitational Waves emitted by binary systems

In this section we shall apply the theoretical quadrupole formalism developed above to study the GW signal emitted by a binary systems, such as two black holes, in circular orbit, referring to [26].

For this purpose, we consider two point masses m_1 and m_2 orbiting around their common center of mass that describe a circular orbit in the x-y plane, as shown in fig (1.3). The orbital frequency ω_K can be found by Kepler's law: $\omega_k = \sqrt{\frac{GM}{l_0^3}}$, where $M = m_1 + m_2$ is the total mass and $l_0 = r_1 + r_2$ the orbital separation between two bodies.
The quadrupole formula (1.26) shows that the main contribution to the gravitational perturbation is given by the second time derivative of the quadrupole moment. Therefore, the non-null components of the quadrupole tensor (1.24) must be computed.
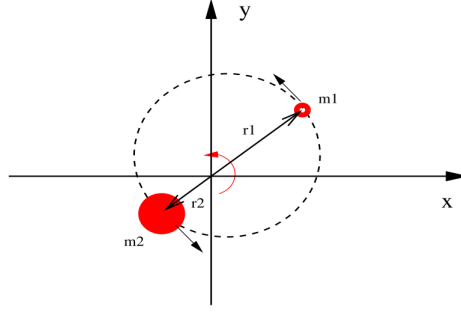In the slow-motion approximation $v << c$, it's true that $p^0 \simeq mc$ and the 00-

Figure 1.3. A simple scheme of a binary system.

component of the stress-energy tensor of the system reduces to:

$$T^{00} = c^2 \sum_{n=1}^{2} m_n \delta(x - x_n)\delta(y - y_n)\delta(z)$$

From the expression of T^{00} and equations of motion for the two bodies, we get to write the components of quadrupole tensor:

$$\begin{cases} q_{xx} = \frac{\mu}{2}l_0^2 cos(2\omega_K t) \\ q_{xy} = \frac{\mu}{2}l_0^2 sin(2\omega_K t) \\ q_{yy} = -\frac{\mu}{2}l_0^2 cos(2\omega_K t) \end{cases}$$

where $\mu \equiv \frac{m_1 m_2}{M}$ is the reduced mass. The calculations leading to this result can be found in the Appendix A.

At this point, it is useful to introduce the *reduced quadrupole moment* Q_{ij}

$$Q_{ij} \equiv q_{ij} - \frac{1}{3}\delta_{ij}q_m^m \tag{1.31}$$

which is traceless by definition; moreover, by defining the matrix A_{ij} as

$$A_{ij} = \begin{pmatrix} cos(2\omega_k t) & sin(2\omega_k t) & 0 \\ sin(2\omega_k t) & -cos(2\omega_k t) & 0 \\ 0 & 0 & 0 \end{pmatrix}$$

we can synthesize the expression of reduced quadrupole moment as

$$Q_{ij} = \frac{\mu}{2}l_0^2 A_{ij} \tag{1.32}$$

The operator $\mathcal{P}_{ijkl}$ now acts on A_{ij}

$$A_{ij}^{\mathbf{TT}}\left(t - \frac{r}{c}\right) = \mathcal{P}_{ijkl}A_{ij}\left(t - \frac{r}{c}\right)$$

and we can finally write the signal emitted at a time t by the binary system located at distance r from the observer as

$$h_{ij}^{\mathbf{TT}}(t,r) = -\frac{h_0}{r}A_{ij}^{\mathbf{TT}}\left(t - \frac{r}{c}\right) \tag{1.33}$$

where h_0 is the instantaneous wave amplitude

$$h_0 = \frac{4\mu M G^2}{l_0 c^4} \tag{1.34}$$

It should be noted that we have achieved an important result: a binary system in circular orbit emits waves at *twice* the orbital frequency, $f_K = \omega_K/2\pi$, as shown by Eq. (1.32)

$$f_{gw} = 2f_K = \frac{\omega_K}{\pi}$$

If $n = z$, $P_{ij} = diag(1,1,0)$

$$A_{ij}^{TT} = \begin{pmatrix} cos2\omega_k t & sin(2\omega_k t) & 0 \\ sin(2\omega_k t) & -cos(2\omega_k t) & 0 \\ 0 & 0 & 0 \end{pmatrix}$$

and

$$h_{xx}^{\mathbf{TT}} = -h_{yy}^{\mathbf{TT}} = -\frac{h_0}{z} cos2\omega_K \left(t - \frac{z}{c}\right)$$

$$h_{xy}^{\mathbf{TT}} = -\frac{h_0}{z} sin2\omega_K \left(t - \frac{z}{c}\right)$$

From $h_{ij}^{\mathbf{TT}}$ we can see that the wave emitted in the direction orthogonal to the orbital plane has both polarizations and it is circularly polarized.
If $n = x$, $P_{ij} = diag(0,1,1)$

$$A_{ij}^{TT} = \begin{pmatrix} 0 & 0 & 0 \\ 0 & -\frac{1}{2}cos(2\omega_k t) & 0 \\ 0 & 0 & \frac{1}{2}cos(2\omega_k t) \end{pmatrix}$$

and

$$h_{yy}^{\mathbf{TT}} = -h_{zz}^{\mathbf{TT}} = +\frac{1}{2}\frac{h_0}{x} cos2\omega_K \left(t - \frac{x}{c}\right)$$

If $n = y$, $P_{ij} = diag(1,0,1)$

$$A_{ij}^{TT} = \begin{pmatrix} \frac{1}{2}cos(2\omega_k t) & 0 & 0 \\ 0 & 0 & 0 \\ 0 & 0 & -\frac{1}{2}cos(2\omega_k t) \end{pmatrix}$$

and

$$h_{xx}^{\mathbf{TT}} = -h_{zz}^{\mathbf{TT}} = -\frac{1}{2}\frac{h_0}{y} cos2\omega_K \left(t - \frac{y}{c}\right)$$

Thus, the wave is linearly polarized along x and y directions.

Finally, we can compute the gravitational wave luminosity given by Eq (1.30) for a binary system, using the expression of the reduce quadrupole (1.32)

$$L_{GW} = \frac{dE_{GW}}{dt} = \frac{32}{5} \frac{G^4}{c^5} \frac{\mu^2 M^3}{l_0^5} \tag{1.35}$$

1.4 Gravitational Waves from Coalescing Black Holes

Let us focus now on a binary system of black holes and on the main features of the emitted gravitational signal.

GWs from BBHs carry information about the properties of the black holes. Theoretically, the waveform $h(t)$ will depend on the parameters that characterize the system. In the case of a non-precessing binary system in circular orbital these parameters are:

- intrinsic parameters: primary mass m_1, secondary mass m_2 and two dimensionless spin angular moment, $\vec{\chi_1}$ and $\vec{\chi_2}$.

- luminosity distance d_L, right ascension ra and declination dec.

- inclination angle between the observers line of sight at the orbital angular momentum ι, polarization angle ψ

- time of coalescence t_c, phase of coalescence ψ_c

BBHs moving in quasi-circular orbits lose orbital energy due to the emission of GW. If we consider to be in a regime where the gravitational energy radiated is balanced by the system by changing its orbital energy [6], we are able to determine analytic relations that describe how the fundamental orbital parameters change over time [26]:

$$
l_0(t) = l_0^{in} \left(1 - \frac{t}{t_c}\right)^{1/4}
$$

$$
\omega_K(t) = \omega_K^{in} \left(1 - \frac{t}{t_c}\right)^{-3/8} \qquad (1.36)
$$

$$
P(t) = P^{in} \left(1 - \frac{t}{t_c}\right)^{3/8}
$$

where t_c is the critical time defined as:

$$
t_c = \frac{5}{256} \frac{c^5}{G} \frac{(l_0^{in})^4}{\mu M^2}
$$

Eqs. (1.36) shows that if $t \to t_c$, then $l_0(t) \to 0$, $\omega_K(t) \to \infty$ and $P(t) \to 0$: as the binary evolves, the emission of gravitational radiation cause orbital separation to shrink until the two black holes merge; on the other hand, the orbital frequency grows. t_c gives a estimate of the time required for merger for a binary with initial orbital separation l_0^{in}; it is called *time of coalescence*.

The *coalescence* of two black holes can be schematized in three distinct phases: the inspiral, the merger and the ringdown (Fig.1.4).

---

[6]This is the *adiabatic approximation*:
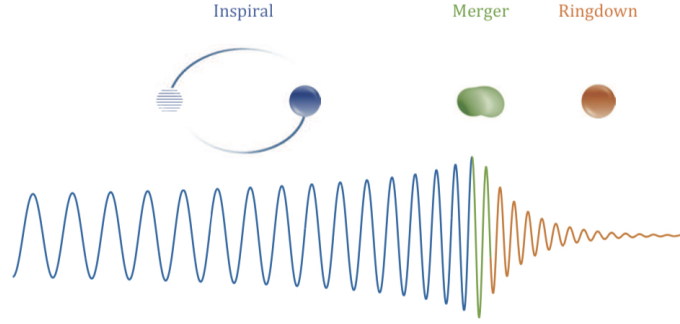
$$
L_{GW} + \frac{dE_{orb}}{dt} = 0
$$

Figure 1.4. Example of the signal emitted by coalescing black holes. The first phase is the inspiral and the GW emitted is a chirp signal, i.e. a sinusoidal wave increasing in frequency and amplitude up to a limit. In the second phase the two objects collide and merge into one. During the third stage, the ringdown, the resulting black hole relaxes to a stationary state. [11]

1.4.1   Inpiral phase: the chirp signal

In the inspiral phase the two objects are orbiting and approaching each other. Many orbits away from the innermost stable circular orbit (ISCO), the inspiral can be approximated as a sequence of stationary circular orbits and the two bodies have an orbital separation that is larger than their extent so they can be treated as two point masses, see also discussion in Sec.(1.3). At this stage, the Newtonian approximation holds and the gravitational-wave signal is described by the laws obtained in Sec.(1.3) through the quadrupole formalism. Furthermore, in Sec.(1.3) it has been demonstrated that the frequency of GW emitted by a binary system is twice the orbital one.

Equating the radiated power due to gravitational wave emission with the rate of change of the orbital energy of the system we arrive at [36]

$$\dot{f}_{gw} = \frac{96}{5}\pi^{\frac{8}{3}}\left(\frac{G\mathcal{M}}{c^3}\right)^{5/3} f_{gw}^{11/3} \tag{1.37}$$

that is the so-called *spin-up*, i.e. the rate of change of the frequency.

The term $\mathcal{M}$ is the **chirp mass** of the system and is defined as

$$\mathcal{M} = \mu^{3/5}M^{2/5} = \frac{(m_1 m_2)^{3/5}}{M^{1/5}} \tag{1.38}$$

Defining a costant K as

$$K \equiv \frac{96}{5}\pi^{\frac{8}{3}}\left(\frac{G\mathcal{M}}{c^3}\right)^{5/3} \tag{1.39}$$

and integrating Eq. (1.37) we obtain the frequency evolution:

$$f_{gw}(t) = f_0\left[1 - \frac{8}{3}Kf_0^{8/3}(t - t_0)\right]^{-\frac{3}{8}} \tag{1.40}$$

where f_0 is the frequency at the initial instant t_0.

The inspiral evolves over a finite time interval, that is, from the initial time t_0 up to the instant immediately preceding the time in which the coalescence takes place, t_c. We define the *time to coalescence* $\tau \equiv t_c - t$ and it can be estimated using the following approximate formula:

$$\tau \sim \left(\frac{1.21 M_\odot}{M_c}\right)^{5/3} \left(\frac{100 Hz}{f_{gw}}\right) \tag{1.41}$$

The phase ϕ of the signal can be obtained by calculating the integral

$$\phi(t) = \int 2\omega_K(t) dt \tag{1.42}$$

and this leads to

$$\phi(t) = -2\left(\frac{c^3(t - t_c)}{5G\mathcal{M}}\right)^{5/8} + \phi_0 \tag{1.43}$$

At the lowest order Newtonian approximation, the phase of the gravitational signal depends on the masses m_1 and m_2 only through the combination given by the chirp mass $\mathcal{M}$.

The temporal evolution of the $+$ and $\times$ polarizations of GW[7] during the inspiral is [36]

$$h_+(t) = \frac{4}{r}\left(\frac{G\mathcal{M}}{c^2}\right)^{5/3}\left(\frac{\pi f_{gw}(t)}{c}\right)^{2/3}\left(\frac{1 + cos^2\iota}{2}\right) cos[\phi(t)] \tag{1.44}$$

$$h_\times(t) = \frac{4}{r}\left(\frac{G\mathcal{M}}{c^2}\right)^{5/3}\left(\frac{\pi f_{gw}(t)}{c}\right)^{2/3} cos\iota sin[\phi(t)] \tag{1.45}$$

These equations show that, as the time increase, both the frequency and the amplitude of the gravitational signal emitted by a binary system during the inspiral increase. This signal is called **chirp**.

The frequency domain representation of the chirp signal is given by calculating the Fourier transform of $h(t)$:

$$\tilde{h}_+(f) = Ae^{i\Psi_+(f)}\frac{c}{r}\left(\frac{G\mathcal{M}}{c^3}\right)^{\frac{5}{6}}\frac{1}{f^{7/6}}\left(\frac{1 + cos^2\iota}{2}\right) \tag{1.46}$$

$$\tilde{h}_\times(f) = Ae^{i\Psi_\times(f)}\frac{c}{r}\left(\frac{G\mathcal{M}}{c^3}\right)^{\frac{5}{6}}\frac{1}{f^{7/6}} cos\iota \tag{1.47}$$

where A is a costant: $A = \frac{1}{\pi^{2/3}}\left(\frac{5}{24}\right)^{1/2}$. The phases are:

$$\Psi_+(f) = 2\pi f t_c - \phi_c - \frac{\pi}{4} + \frac{3}{4}\left(\frac{G\mathcal{M}}{c^3}8\pi f\right) \tag{1.48}$$

and $\Psi_\times = \Psi_+ + (\pi/2)$; Φ_c is the value of the phase at coalescence.
The quadrupole approximation is not sufficient to correctly determine the intrinsic

---

[7]We have omitted the time delay between signal emission and detection

parameters of the system. In fact, Eqs. (1.44), (1.45) and 1.43 show that the masses of the system do not appear separately, but only via the chirp mass parameter. The chirp mass allows us to establish limits for the total mass of the binary system but not to identify the two masses individually. Furthermore, the bodies have been approximated as point-like and consequently the contribution of the spins is not taken into account.

In order to obtain a more accurate description of the waveform, the Post-Newtonian approximation is used.

1.4.2 Post-Newtonian expansion

The quadrupole approximation is appropriate to describe the signal evolution as long as the two bodies are far from the innermost stable circular orbit, the ISCO.

$$r_{ISCO} = \frac{6GM}{c^2} \tag{1.49}$$

corresponding to the frequency [36]

$$f_{ISCO} = \frac{1}{6\sqrt{6}(2\pi)}\frac{c^3}{GM} \tag{1.50}$$

When the two bodies approach the ISCO, it is necessary to consider the contribution of Post-Newtonian effects, i.e. corrections of a certain order to the Newtonian waveform. Post-newtonian waveform include corrections to the expressions of amplitude, energy and luminosity of GW. In particular, the post-Newtonian corrections to the energy $E(r)$ modify the speed during the inspiral and this is very important to estimate the accumulated orbital phase $\phi(t)$. [22]

Customarily, the term $P^x N$ of the expansion indicates that the corrections to the quadrupole formule are of order x: $x = (v/c)^2$.

The most of information that allows significant measurement of the masses of the bodies is accumulated in the phase evolution of the signal. For this reason, rather than use the full Post-Newtonian waveform, the "model" waveform is calculated as follows

$$h(t) = h_0(t)e^{2i[\psi^0 + \psi^1 + \psi^{1.5} + \psi^2 + ..]} \tag{1.51}$$

where h_0 is the amplitude to the lower order, i.e the quadrupole formula. Thus, the waveform $h(t)$ assumes that amplitude evolution in given by quadrupole formula but includes higher-order terms corrections to the phase.

The first correction $P^1 N$ to the phase includes the parameters of reduced μ and total mass M which allow to completely solve the individual masses of the binary system. The terms $P^{1.5} N$ and $P^2 N$ carry information on the effect of the spins of the binary components. This spin corrections become important where the two objects get close because strong field effects take place.

The evolution of the phase in the P^2N approximation is [11]:

$$\psi(f) = 2\pi f t_c - 2\phi_0 - \pi/4 + \frac{3}{128\eta}[v^{-5} + \left(\frac{3715}{756} + \frac{55}{9}\eta\right)v^{-3} - 16\pi v^{-2} + \\ + \left(\frac{15293365}{508032} + \frac{27145}{504}\eta + \frac{3085}{72}\eta^2\right)v^{-1}] \tag{1.52}$$

where

$$v = (\pi M f G/c^3)^{1/3} \tag{1.53}$$

1.4.3   Merger and ringdown

When the orbital separation of the two black holes reaches the ISCO, the merger phase begins. The system is dynamically unstable and the two black holes plunge and merge. At this stage, strongly non linear effects dominate, thus the linearized theory is no longer valid and Einstein's field equations must be solved numerically. The aim of Numerical Relativity (NR) is to compute the collision of two black holes and obtain the waveforms expected according to initial conditions.

The final result of the merger is a Kerr Black Hole with a spin given by the total angular momentum of the binary system, which oscillates due to its asymmetric shape. This is the ringdown stage. The GW emitted signal decays as a superposition of its quasi-normal modes (QNM) of oscillations and it is described by damped sinusoid:

$$h(t) = \sum_i A_i sin(\omega^i t + \phi^i)e^{-\frac{t}{\tau}} \tag{1.54}$$

where ω depends on the mass and spin of the final black hole. Although it has recently been demonstrated that correct modelling of the ringdown stage, which improves mismatches by an order of magnitude, requires the inclusion of non-linear effects [39].

As well as the inspiral, also the ringdown phase is well modeled by perturbative techniques.

1.5   Gravitational Waves Detection

The passage of a gravitational wave induces length variations of the order typically smaller than $h \sim 10^{-19}$. Attempting to measure these tiny deformations means that the instrument must be extremely sensitive. The scientific instrument capable of carrying out these very small measurements is the laser interferometer.

A gravitational wave detector consists of an L-shaped Michelson interferometer with 4 km long arms, a Fabry Perot cavities and power recycling systems. The basic mechanism is as follows: a laser beam hits a beam splitter, which divides the beam into two perpendicular beams. Each beam of light is then reflected by mirrors, placed at the end of the arm, towards the beam splitter where they are added together. The resulting laser light is then collected with a photodiode.

If a GW signal arrives, the length of the arms varies and the optical path of each light beam also changes. This leads to a different time travel of the light in the arms and the two laser lights will superimpose with a varying phase when recombined to the beam splitter. This phase variation translates in a changing light interference pattern at the detector output, which is actually measured through the force which must be applied to the mirrors to keep the interferometer at a fixed working point.

A Fabry-Perot cavity adds to the basic design of a Michelson interferometer to achieve the sensitivity required to measure GW; it consists of mirrors placed in the arms near the beam splitter. These mirrors are designed to reflect light multiple times in order to increase the phase shift to measurable values.

The energy recycling system aims to increase the effective laser power stored in the arms in order to improve its detector sensitivity, without increasing the power of the laser source. This system is based on a "recycling mirrors", located between the beam splitter and the laser source, that reflects the laser light received from the arms back to the beam splitter.

Fig.(1.5) is a representation of the optical layout of Advanced Virgo during the run O3.

Actual detectors of GW are LIGO (Laser Interferometer Gravitational-Wave Observatory) one located at Livingston (referred as L1) and one at Hanford (H1), in USA, and Virgo at Cascina in Italy. At the end of run O3 the underground and cryogenic detector KAGRA (KAmioka GRAvitational wave telescope) it started to work, although with low sensitivity, in Japan. A third LIGO interferometer will be placed in India and operated by the Indian Initiative in Gravitational-wave Observations (IndIGO) in the future.

The detectors are required to be located in separate locations to validate and confirm GW events by coincident detections and to estimate the position of the source in the sky. In fact, at least for short duration signals, the position of the source is determined by the differences in the arrival times of the signal in three widely separated detectors. For long duration signals the sky location of the source can be determined through the Doppler effect due to the Earth motion, which impacts on the signal at the detector, as we will explain in Sec. (4.2).
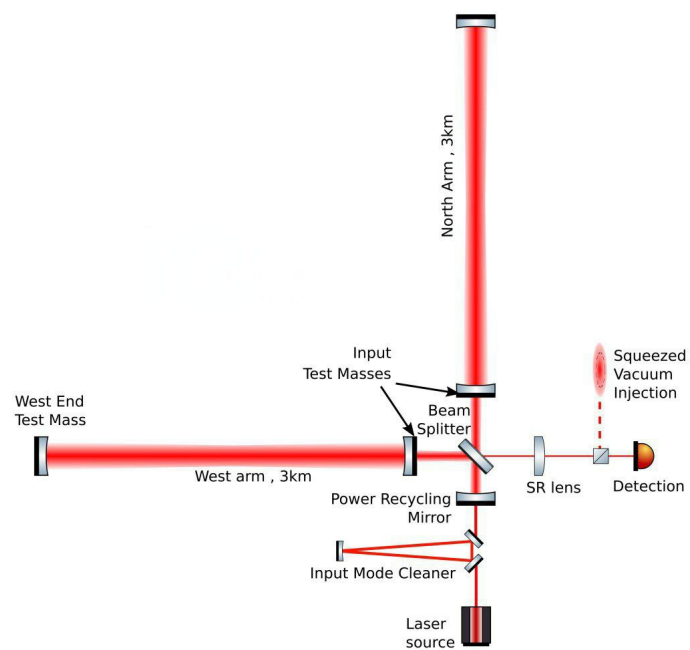
Figure 1.5. Illustration of Virgo interferometer configuration with the main components. http://public.virgo-gw.eu/advanced-virgo/

Chapter 2

Primordial Black Holes

Primordial Black Holes (PBH) could form in the early Universe from the collapse of large density perturbations. PBHs are sources of great interest because they differ from astrophysical black holes in their cosmological origin. They represent a candidate for one of the components of the dark matter (DM) in the Universe.
PBHs can assemble in binaries leading to observable signals at current LIGO and Virgo detector.
In this chapter we will discuss some basics on PBHs formation and characterics and will provides estimations of rates at which PBH binaries will merge. In the second part, we will show how recent studies have been able to constrain PBH abundance, in some mass ranges, through GW signals observed by the LIGO/Virgo collaboration (LVC).

2.1 PBHs formation and mass distribution

The idea that PBHs could form in the early Universe appeared for the first time in the works of *Zel'dovich* and *Novikov (1966)* [49] and *Hawking (1971)* [29].
Unlike black holes that form from the collapse of massive stars, PBHs could have formed in the early Universe from the collapse of large density perturbations.

The mass of a forming black hole in the early Universe depends on its time of formation. Since the cosmological density at a time t after the Big Bang is $\rho \sim 1/(Gt^2)$ and the density required for a region of mass M to fall within its Schwarzschild radius is $\rho \sim c^6/(G^3M^2)$, PBHs would initially have mass around the cosmological horizon

$$M_H \sim \frac{c^3 t}{G} \sim 10^{15} g \frac{t}{10^{-23}s} \tag{2.1}$$

that is the mass within the Hubble horizon at that time [17]. This means that PBHs could cover an enormous range of masses: those formed at Planck time (10^{-43} s) would have the mass of Planck (10^{-5} g), while those formed at 1 s would be as large as $10^5 M_\odot$, comparable to the mass of the holes thought to reside in galactic nuclei and $1 M_\odot$ if they formed at the QCD (Quantum chromodynamics) epoch (10^{-5} s).

There are various possible scenarios which have been proposed for PBH formation; here we give here a few examples, following [17]. Furthermore, depending on the specific formation mechanism of the PBH population, different mass distributions can be expected, as it is determined by the specific form of the fluctuation increase. The mass distribution, $\psi(M)$, representing the mass fraction of PBHs with mass within $(M, M + dM)$ [16]

$$\psi(M) \propto M \frac{dn}{dM} \tag{2.2}$$

where M is the PBH mass, dn is the number density of black holes within the mass range $(M, M + dM)$ and dn/dM is the so-called mass function.
The mass distribution is normalised so that the fraction of the DM in PBHs is

$$f_{PBH} \equiv \frac{\Omega_{PBH}}{\Omega_{DM}} = \int dM \psi(M) \tag{2.3}$$

where Ω_{PBH} and Ω_{DM} are the PBH and DM den- sities in units of the critical density.

We have seen that PBHs generally have a mass of the order of the horizon mass at formation, so one might expect a monochromatic mass function i.e. with a width $\Delta M \sim M$. However, in some scenarios PBH are formed over a prolonged period and thus have an extended mass function [16], e.g. with the shape of the mass function depending on the power spectrum of the primordial fluctuations.

Primordial inhomogeneities The most naturally possibility is that PBHs could arise from the collapse of large density perturbations in the early Universe. Regardless of the source of the density fluctuations, they would have to be larger than the Jeans length at maximum expansion in order to collapse against pressure. Because the background pressure is very large during the radiation dominated era, $P = \rho \omega c^2$, this means that only large-amplitude perturbations will have a gravitational attraction strong enough to overcome the pressure forces and collapse into a black hole. One can use a Jeans length arguments in Newtonian gravity to derive a simple order of magnitude estimate for the threshold beyond which an overdensity can collapse. Defining the density contrast as $\delta = \delta\rho/\rho$, the first estimate for the collapse threshold for PBH formation was made by *Carr (1975)* in [18] using the Jeans' length and time and using Newtonian gravity, who found that an overdensity would collapse if its density contrast is

$$\delta_c \sim c_s^2 \tag{2.4}$$

where $c_s^2 = 1/3$ is the speed of sound at the radiation epoch. δ_c is the *collapse threshold*. The fluctuations are characterized by the power spectrum $|\delta_k|^2 \sim k^n$, where n is the spectral index.

Collapse from scale-invariant fluctuations If PBH are formed from scale invariant fluctuations, i.e. with constant amplitude at the horizon epoch, their mass spectrum should have the following power-law form [16]

$$\psi(M) \propto M^{\gamma-1} \tag{2.5}$$

where $\gamma = -2\omega/(1+\omega)$, where ω specifies the equation of state when the PBHs form. It was once argued that primordial fluctuations would be scale invariant, but this argument does not apply in the inflationary scenario. [28]

Crtical collapse It is well known that the formation of black holes is associated with critical phenomena. When the mass of the density perturbation approaches the threshold value δ_c required for PBH formation, a critical phenomenon occurs, which is referred to as critical collapse and which can occur, for example, at QCD times. If we assume for simplicity that the density fluctuations have a monochromatic power spectrum on a certain mass scale K, the mass of PBHs is related to the mass contained in the horizon, at the time of formation t_f, through a factor γ [20]

$$M = K(\delta - \delta_c)^\gamma \tag{2.6}$$

where K can be identified with a mass of the order the horizon mass and thus extends to arbitrarily small scales. A detailed calculation found in [48] gives the mass function following the relation

$$\frac{dn}{dM} \propto \left(\frac{M}{\xi M_f}\right)^{1/\eta - 1} exp\left[-1(1-\eta)\left(\frac{M}{\eta M_f}\right)^{1/\eta}\right] \tag{2.7}$$

where $\xi \equiv (1 - \eta/s)^\eta$, $s = \delta_c/\sigma$, σ is the dispersion of δ and $M_f = K$.

Collapse from inflationary fluctuations The most natural source of fluctuations should be quantum effects during inflation. In the simplest case, with only one scalar field, the inflationary fluctuations depend on the shape of the inflatonic potential $V(\phi)$ and should have a power-law shape. A different mechanism for PBH production occurs in multi-field scenarios. In this case, the inflationary field is given by the contribution of two fields: one of the fields ϕ initially slow-rolls and the second one ψ drives the accelerated expansion.
Observations show fluctuations generated by inflation have a red spectrum, implying that the spectral index should change on a smaller scale to generate PBH.

Alternatively, the PBHs could form from a smooth symmetric peak in the inflationary power spectrum, in which case the PBH mass function should have the following log-normal form

$$\psi(M) = \frac{f_{PBH}}{\sqrt{2\pi}\sigma M} exp\left(-\frac{log^2(M/M_c)}{2\sigma^2}\right) \tag{2.8}$$

Eq. (2.8) implies that the mass function is symmetric with respect to its peak at M_c and described by two parameters: the mass scale M_c itself and the width of the distribution σ. This form was first proposed in [24] and has been proven both numerically and analytically for the case where the slow-rolling approximation holds. It is thus representative of a broad class of inflationary scenarios.

Collapse in a matter-dominated era   Whatever the source of the inhomogeneities, the formation of PBH would be favoured if some phase transition led to a sudden reduction in pressure, e.g. if the primordial Universe soon went through a dusty phase, having been dominated by non-relativistic particles for a period, or if it slowly warmed up after inflation. In this case pressure is not the main inhibitor of collapse but instead is inhibited by deviations from spherical symmetry and the probability of PBH formation can be demonstrated as follows

$$\beta(M) = 0.056\sigma(M)^5 \tag{2.9}$$

If the matter-dominated phase extends from t_1 to t_2, PBH formation is enhanced over the mass range

$$M_{min} \sim M_H(t_1) < M < M_{max} \sim M_H(t_2)\sigma(M_{max})^{3/2} \tag{2.10}$$

where M_H horizon mass at the start of matter dominated era. This scenario has been stutied in [16].

Collapse at QCD phase transitions   One possibility is that PBHs with a mass of about $1M_\odot$ may have formed at the quark-hadron phase transition at 10^{-5}s due to a temporary softening of the equation of state. If the QCD phase transition is assumed to be of the first order, meaning that quark-gluon and hadron plasma phases could coexist, calculations show that the δ value required for PBH formation is actually reduced below the value occurring in the case of radiation. This means that the formation of PBH will be strongly enhanced at the QCD epoch, with a peak in the mass distribution around the horizon mass. One of the interesting implications of these scenarios is the possible existence of a halo population of binary black holes. With a complete halo of such objects, there could be a huge number of binaries and some of these could coalescence due to gravitational radiation losses at the present time. If the associated gravitational waves were detected, they would provide a unique probe of the halo distribution.
PBH formation during a first-order QCD phase transition was first suggested in [21] and later in [32].

2.2   PBHs spins

One parameter that can be a good proxy for distinguishing the nature of a BH population is spin. Astrophysical BHs are expected to have essentially large spins, since the angular momentum must be conserved during the collapse of the source stars, which are often rotating. This is not the case for PBHs since, if we consider the isotropy principle, the total spin of the density perturbation is null. Therefore, we expect PBHs to have no spin or a slight spin provided by the influence of other compact objects, of the order of ~ 0.01 [23]. The spin parameter is measurable from the merger of binary black holes in LIGO and Virgo. The latest Bayesian analyses of the LIGO/Virgo mergers [27] suggest that for as a homogeneous population of black holes, low spins with isotropic orientations, are strongly favoured by the data, regardless of the assumed priors.

2.3   Abundance of PBHs

One important point is that observations imply that only a tiny fraction of the fluctuations in the early Universe could have collapsed into PBHs.

The initial abundance β of PBHs at the time of formation β, i.e. the fraction of the mass of the Universe in PBHs, can be defined as

$$\beta = \frac{\rho_{PBH}(t_f)}{\rho_{tot}(t_f)} \tag{2.11}$$

where ρ_{PBH} is PBH density and ρ_{tot} is density at time formation. Taking into account all overdensities above the collapse threshold, and assuming a Gaussian probability distribution $P(\delta)$ for overdensities with variance $\sigma^2(M)$ at a mass scale M, β is the probability that the density contrast δ overcomes the threshold δ_c:

$$\beta(M_{PBH}) \sim \gamma \int_{\delta_c}^{\infty} P(\delta)d\delta \simeq \gamma \sqrt{\frac{2}{\pi}} \frac{\sigma(M_{PBH})}{\delta_c} exp\left[-\frac{\delta_c^2}{2\sigma^2(M_{PBH})}\right] \tag{2.12}$$

The assumption of a Gaussian distribution is not realistic, but it is useful to give an idea of the magnitude of the fluctuation amplitude; for the standard cosmological scenario with an initial scale invariant power spectrum, this leads to $\sigma(M_{PBH}) \sim 10^{-5}$ and $\beta \sim 10^{-5} \exp(-10^{-10})$. However, although the initial fraction β is very small, since matter and radiation densities scale differently with redshift, as $(1+z)^3$ and $(1+z)^4$ respectively, the contribution of PBHs can become relevant at present times. The current density parameter Ω_{PBH} associated with PBHs that form at a redshift z is related to the initial collapse fraction β by

$$\Omega_{PBH}(M) = \beta(M)(1+z)\Omega_R \tag{2.13}$$

where $\Omega_R \sim 10^{-4}$ is the density parameter of the microwave background radiation.

2.4   Evaporation of PBHs

An important phenomenon of BHs is that of evaporation. Due to quantum effects in curved spaces, BHs can emit particles at their event horizon. This is the famous discovery of Hawking [30] that black holes radiate thermally and the radiation emitted would have a quasi-thermal blackbody spectrum, with a temperature given by

$$T_{BH} = \frac{\hbar c^3}{8\pi k_B GM} \sim 10^{-7} K \frac{M_\odot}{M} \tag{2.14}$$

which is known as the Hawking temperature. Due to this emission, BHs slowly lose mass until they evaporate completely. They evaporate completely on a timescale

$$\tau(M) \sim 10^{64} yr \left(\frac{M}{M_\odot}\right) \tag{2.15}$$

Therefore, the lower the mass of PBH, the sooner it evaporates. Those with masses of 10^{15} g or less would have already evaporated, so they cannot contribute to the current abundance of DM. These evaporation products or the effects they produce in different observables can be researched in a variety of experiments, probing different mass ranges.

2.5 PBH Merging Rate

To determine the merger rate of PBHs, one must first consider the number density of PBHs of a given mass, which is related to the mass distribution $\Psi(M)$, and then the fraction of these that can form binaries. [38]. There are different possible channels for the formation of PBH binaries that would result in different merger rates, described in [38]. The cosmological merger rate today is:

$$R_{cosm} \equiv \frac{d\tau}{dlog(m_1)dlog(m_2)} \tag{2.16}$$

where τ is the rate per unit of logarithmic mass of the two binary components m_1 and m_2.

The first formation channel assumes that binary formation begins when the Newtonian gravitational attraction of close PBHs exceeds the effect of cosmic expansion, before matter-radiation equality in the primordial universe.

In this case, the cosmolgical merger rate is estimated by assuming that the spatial separation of PBH at the time of formation is Poissonian, and it is today given approximately by

$$R_{prim} \approx \frac{1.6^6}{Gpc^3yr} f_{sup} f_{PBH}^{53/37} \left(\frac{m_1 + m_2}{M_\odot} \right)^{-32/37} \times \left[\frac{m_1 m_2}{(m_1 + m_2)^2} \right] f(m_1)f(m_2) \tag{2.17}$$

where f_{PBH} is the dark matter density fraction made of PBHs and $f(m)$ is the normalized density distribution of PBHs. A suppression factor f_{sup} is included in the equation (2.17) to account for rate suppression due to the gravitational influence of early-forming PBH clusters.

Since the focus of this thesis is on GWs from PBH binaries located in the Galactic centre, the merging rate can be evaluated in the Milky Way, towards the galactic center or in the solar system vicinity, by integrating (2.17) and assuming an Einasto dark matter halo profile, this leads to:

$$R_{prim}^{gal} \approx 2.2 \times 10^{-8} \times R_{prim}^{cos} \tag{2.18}$$

$$R_{prim}^{GC} \approx 1.1 \times 10^{-13} \times R_{prim}^{cos} \tag{2.19}$$

$$R_{prim}^{sol} \approx 1.1 \times 10^{-21} \left(\frac{d}{pc} \right)^3 \times R_{prim}^{cos} \tag{2.20}$$

where d is the considered maximal distance of the PBH binary. The number of PBH binaries is approximately given by

$$N_{prim}^{gal/GC/sol} \approx R_{prim}^{gal/GC/sol} \times t_{merg} \tag{2.21}$$

because it must be taken into account that, for small chirp mass values and lower frequencies, continuous waves are emitted long before binary fusion, which may last many years, so the number of current binaries may be greater than one even if the rate is $R_{prim} \ll \text{yr}^{-1}$.

The second possible channel of binary formation is the dynamic capture in dense PBH halos. Like any other dark matter candidate, PBHs are expected to form halos in the course of cosmic history. Their clustering properties determine the corresponding merging rate, and the cosmological merging rate is approximately given by:

$$R_{capt}^{cos} \equiv \frac{d\tau}{dlog(m_1)dlog(m_2)} \approx R_{clust}f_{PBH}f(m_1)f(m_2)\left[\frac{m_1+m_2}{(m_1m_2)^{5/7}}\right]^{-32/37} \quad (2.22)$$

where R_{clust} is a factor that incorporates the PBH clustering properties and it is strongly model-dependent. The recent events GW190425 and GW190814 with a suspected object in the black hole mass gap can be explained for a value of $R_{clus} \approx 400yr^{-1}$ Gpc^{-3}, for $f_{PBH} = 1$.

2.6   Gravitational waves from primordial black holes

PBHs can impact cosmology and astrophysics in different ways, producing several effects which allow to constrain the abundance of PBHs in our galaxy, and so the fraction of dark matter. The figure (2.1) shows a list of existing constrains from different studies on the fraction of dark matter that can be thought to compose PBHs. Since constraints on the PBH population require a model to connect the abundance and mass distribution of PBH to the rate of mergers observed, most previous works assumed that the PBH mass function is monochromatic. This greatly simplifies the problem, but it is likely unrealistic.

The observations of GWs from black hole mergers by LIGO and Virgo Collaboration can be employed to constrain the allowed number of PBHs, by requiring the number of detectable PBH events per year not to exceed the observed rate. Constrains have been found in [38], where it is argued that the current research of continuous waves from PBH binaries implies $f < 1$ for chirp masses in the range between $4 \times 10^{-5} M_\odot$ and $10^{-3} M_\odot$, but one could stretch this limit to $f < 10^{-2}$ with the Einstein Telescope. Complementary constrains are found in [46], from the stochastic gravitational-wave background due to PBH mergers in the range of $[10^{-8}, 1]M_\odot$.

Stellar evolution models predict that black holes only form when the mass of a star is sufficient for the gravitational force to overcome the degeneracy pressure. A mass below $1M_\odot$ is a clear PBH signature, since these black holes cannot possibly originate from stellar evolution [19]. However, the LIGO/Virgo runs have found no compact binary systems with component masses in the range $0.2 - 1.0M_\odot$. Indeed, for monochromatic non-spinning PBHs, the merger rate of $0.2M_\odot$ and $1.0M_\odot$ binaries is constrained to be less than $3.7 \times 10^5 \ Gpc^{-3}yr^{-1}$ and $5.2 \times 10^3 \ Gpc^{-3}yr^{-1}$, respectively [3]. In [6], LVK reports the search from O3a for compact binaries in which at least one of the component objects had a mass between $[0.2 - 1.0]M\odot$. Here the analysis is extended to a greater number of systems with unequal mass, compared to the previous analysis. No candidates were found and upper limits were

obtained on the merger rate of black holes of subsolar mass in the range [220 -24200] $Gpc^{-3} \ yr^{-1}$.
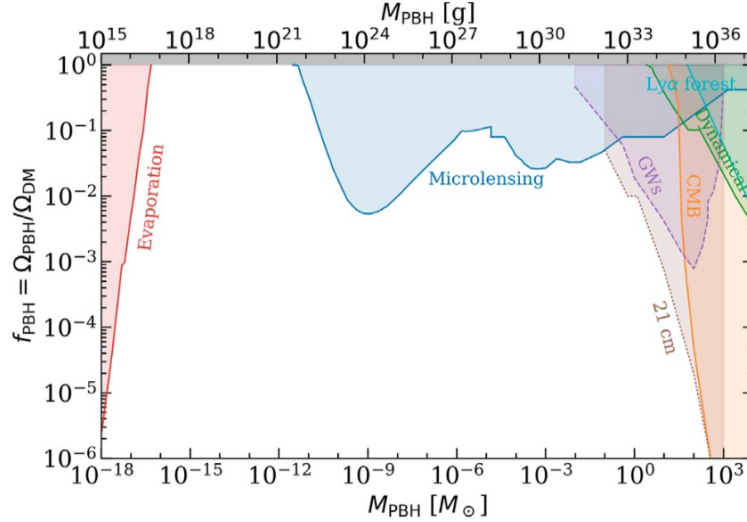

Figure 2.1. Set of constraints on the fraction of PBH contributing to DM as a function of PBH mass, assuming a monochromatic mass function. [1]

However, regardless of the relation to cosmological dark matter, the confirmation of a primordial origin for any black hole would carry great implications, and the detection of even one such object would be decisive. In current and future observation runs of LIGO/Virgo, we will be able to even make a detection of PBH inspirals within our galaxy, if they exist.

Due to large theoretical uncertainties, searches for gravitational signals from PBH aim to cover the widest possible range of masses.
In this thesis, we focus on sub-solar PBHs with masses in the range $[10^{-5} - 10^{-3}]M_\odot$. Due to their extremely small masses, PBHs are expected to inspiral for very long times compared to typical LIGO/Virgo binary black hole signals, potentially for months or years. Therefore, PBH inspirals are ideal candidates for continuous- wave and transient continuous-wave searches. In Chapter 4, I will describe a data analysis procedure tailored to the search for such signals. First of all, some preliminary considerations are necessary, which will be discussed in the next Chapter.

Chapter 3

Preliminary considerations

The first part of my work aims at proving that the GWs from PBH binaries, during the inspiral phase, are well described by perturbative theory with the quadrupole approximation hypothesis. If this is achieved, we can model these GW signals through the formalism described in section (1.4.1). As we said previously, the quadrupole approximation represents the 0th-order term of the PN expansion. This means that if one wants to demonstrate that the quadrupole approximation is good for the analyzed signals, one has to show that the higher-order contributions of the PN expansion have a negligible impact on the signal phase. With this purpose, the so-called *"phenomenological waveforms"* are employed. It should be stressed that here only the inspiral stage is considered, and the ringdown and merger phases are not taken into account. As we explained in Sec. (1.4.2), the inspiral phase ends when the source frequency approaches the value of f_{ISCO}. Inserting the numerical values in Eq. (1.50), this gives: $f_{ISCO} \simeq 2.2 kHz (M_\odot/M)$. Therefore, for sub-solar mass PBH binaries the f_{ISCO} assumes very high value, of the order typically larger than $f_{ISCO} \simeq 10^6$ Hz. For this reason, we can limit the analysis to the early ispiral and, as I will show below, we will choose a reasonably low cut-off frequency.

As a second step, the signal-to-noise ratio will be studied in order to focus on a specific frequency band, relevant for the analysis of the signals, and capable of limiting the computational cost.

3.1 Phenomenological Waveforms: IMR

3.1.1 IMR Waveforms for nonprecessing binaries

We employ a phenomenological framework in order to provide a waveform model for the GW signals from PBH binaries.

The phenomenological waveform are written in the Fourier domain in the following form [43]:

$$\tilde{h}(f; \vec{\lambda}, \vec{\theta}) = \tilde{A}(f; \vec{\lambda}) e^{i\Phi(f; \vec{\theta})} \tag{3.1}$$

where $\vec{\lambda}$ and $\vec{\theta}$ are phenomenological parameters in the amplitude and in the phase respectively. The amplitude and phase are modeled separately. The inspiral stage is

modeled based on analytic PN information, calibrated for example to *Effective One Body (EOB)*[1] results.

A BBH system is described by the following parameters [5]. The masses of two black holes are indicated with m_1 and m_2, with $m_1 \geq m_2$, and the corresponding total mass is $M = m_1 + m_2$. The mass ratio is

$$q = \frac{m_2}{m_1} \leq 1$$

and the symmetric mass ratio is

$$\eta = \frac{m_1 m_2}{M^2}$$

The spin angular momentum $S_{1,2}$ of the binary components are defined in term of the dimensionless spin magnitude

$$a_{1,2} = \frac{c}{G m_{1,2}^2} |S_{1,2}|$$

and the component aligned with the orbital angular momentum $\vec{L}$ is:

$$\chi_{1,2} = \frac{c}{G m_{1,2}^2} |S_{1,2}| \cdot \hat{L}$$

with $\chi_i \in [-1, 1]$. Any misalignment between the spins and the orbital angular momentum induces relativistic precession effects, which cause the orbital plane to change its spatial orientation as the binary evolves. For simplicity, we consider only the case in which the spins are aligned (or anti-aligned) with the orbital angular momentum. So, we use a IMR waveform family for nonprecessing binaries. In this case, the waveform family is parameterized by only the total mass M, the symmetric mass ratio η and a single spin parameter:

$$\chi \equiv \frac{(1+\delta)\chi_1}{2} + \frac{(1-\delta)\chi_2}{2} \tag{3.2}$$

where

$$\delta \equiv \frac{m_1 - m_2}{M} \tag{3.3}$$

In order to track the evolution of the GW signal, we need a template which reconstructs the phase of the signal including the high-order terms of PN. We can understand this observing that the last term in the expression of the phase given by Eq. (1.48) in terms of v is:

$$\frac{3}{4} \left(\frac{G M_c}{c^3} 8\pi f \right)^{-5/3} = \frac{3}{128\eta} v^{-5/2} \tag{3.4}$$

---

[1]The Effective One Body formalism is an analytical approach that aims to provide an accurate description of the coalescence of binary black holes with an arbitrary mass ratio.

This means that for small v the Newtonian phase Ψ is of the order of $v^{-5/2}$ and diverges for $v \to 0$. The P^1N corrections gives a contribution to Ψ of the order $v^{-3/2}$ that still diverges as $v \to 0$ and similarly all the contributions up to $P^{2.5}N$ diverge or stay finite in the small v limit; only starting for P^3N level we have correction which vanish as $v \to 0$. We have to demonstrate that in the case of signal we are studying the higher-order terms are finite and small respect the the term of $0th$-order.

Following [45], the phase of the phenomenological waveform for non-precessing binaries is written, in the Fourier domain, as

$$\Psi = 2\pi f t_0 + \psi_0 + \frac{3}{128\eta v^5}\left(1 + \sum_{k=2}^{7} v^k \psi_k\right) \tag{3.5}$$

where t_0 is the time of arrival of the signal at the detector, ψ_0 the corresponding phase, and v is defined in the same way as Eq. (1.53).

The terms ψ_k are phenomenological parameters depending on the physical parameters of the binary

$$\psi_k = \psi_k^0 + \sum_{i=1}^{3}\sum_{j=0}^{N} x_k^{(ij)}\eta^i\chi^j \tag{3.6}$$

where Ψ_k^0 are the (P^2N) Fourier domain phasing coefficients for a test-particle, N is the minimum of (3-i, 2), and $x_k^{(ij)}$ are phenomenological parameters tabulated below.

ψ_k	(ψ_k^0)	$x^{(10)}$	$x^{(11)}$	$x^{(12)}$	$x^{(20)}$	$x^{(21)}$	$x^{(30)}$
ψ_2	3715/756	-920.9	492.1	135	6742	-1053	-1.34·10^4
ψ_3	-16π+ 113χ/3	1.702·10^4	-9566	-2182	-1.214·10^5	2.075·10^4	2.386 ·10^5
ψ_4	15293365/508032-405χ^2/8	-1.254·10^5	7.507·10^4	1.338·10^4	8.735·10^5	-1.657·10^5	-1.694·10^6
ψ_6	0	-8.898·10^5	6.31·105	5.068·10^4	5.981·10^6	-1.415·10^6	-1.128·10^7
ψ_7	0	8.696·10^5	-6.71·10^5	-3.008·10^4	-5.838·10^6	1.514·10^6	1.0891·10^7

These waveforms are constructed in such a way that they match P^2N adiabatic inspiral waveforms in the test-mass limit, i.e. $\eta \to 0$. In this limit, $\psi_k \to \psi_k^0$.

We now estimate the phase defined in Eq.(3.5) for a chirp mass of $M_c = 10^{-3}M_\odot$, that is the maximum of the considered range mass, and for a frequency of $f = 120$ Hz. The choice of f = 120 Hz will be justified in the next section through the study of the signal-to-noise ratio.

Since for PBHs the dimensionless spin parameter is expected to be lower than 0.01 [1], we consider $\chi_{1,2} = 0.01$. Due to the definition of v, if the post-Newtonian terms are negligible for high mass and frequency the same will be true for any smaller mass and frequency.

With this choice, the PN correction amounts to:

$$\left(\sum_{k=2}^{7} v^k \psi_k\right) \sim 0.01 \ll 1 \tag{3.7}$$

and then it is negligible with respect to the 0th-order term of the PN expansion. In standard scenarios, the spin of primordial black holes is expected to be very small, as explained in Sec. (2.2). However, if we consider that the spin of a black hole may evolve over the cosmic time due to phenomena such as accretion, and we assume, for example a value of $\chi = 0.9$, the PN correction in Eq. (3.7) becomes ~ 0.08, which is still much smaller than the dominant contribution given by $0-$order. As a consequence, we can use the quadrupole approximation to model the inspiral signal emitted by sub-solar mass PBH binaries.

This is an important preliminary result, because the quadrupole approximation allows to reduce the space parameter: the waveform will not depend on the full 15 parameter space for typical of solar mass CBC signals, but only on 4 parameters, i.e. the chirp mass, the reference time t_0, the initial frequency f_0, and the distance d. Using this reduced parameter space is very convenient, because it allows to limit the computational cost of the analysis.

3.2   Filtering and signal-to-noise ratio

The purpose of this section is to show that it is possible to limit the search to low frequencies, without significant losses of signal-to-noise ratio. This leads, at the same time, to a sensitivity improvement and a gain in terms of computational cost.

The output of any GW detector is a time series which contains the strain amplitude induced by the passage of a GW. This output will be a combination of a true GW signal and the noise

$$i(t) = h(t) + n(t) \tag{3.8}$$

$h(t)$ is the signal and $n(t)$ a stochastic variable, describing the detector noise. Ideally the noise of GW detectors can be described by a stationary and Gaussian stochastic process, although deviations from these assumptions often occur in practice.
The noise is typically much larger than the GW signal, so the fundamental problem is how we can extract the signal of the interest. The basic idea is the "filtering" procedure. In particular, the matched filtering technique is the best linear filter to extract a signal of known form swamped in stationary gaussian noise. [31] [10].
It relies on a very accurate knowledge of the signal shape and, if this is not the case, it requires a template bank covering the signal parameter space in such a way as not to degrade the sensitivity of the filter sensitivity too much due to a mismatch between the signal's waveforms and the template.

The performance of a filter can be quantified by means of the signa-to-noise-ratio, which is the ratio among the power of the filtered signal and of the noise.
The output signal $o(t)$ is the result of the convolution of $i(t)$ with the filter function

$k(t)$

$$o(t) = \int_{-\infty}^{\infty} i(t - \tau)k(\tau)d\tau \qquad (3.9)$$

where $k(t)$ corresponds to the response of the filter to an impulse (which can mathematically be written under the form of a delta function) and for this reason it is called *filter impulsive response*. Considering that $i(t)$ is the sum of signal and noise, we can write:

$$o(t) = i(t) \otimes k(t) = [h(t) + n(t)] \otimes k(t) = o_h + o_n$$

where

$$o_h = \int_{-\infty}^{+\infty} h(t - \tau)k(\tau)d\tau$$

$$o_n = \int_{-\infty}^{+\infty} n(t - \tau)k(\tau)d\tau$$

Working in the frequency domain simplifies the study of the filter. We obtain the mapping functions, that convert the signals from the time domain to the frequency domain, applying the Fourier Transform (FT). We write the FT for the functions $i(t)$, $k(t)$ and $o(t)$ as:

$$\mathcal{I}(\omega) = \int_{-\infty}^{+\infty} i(t)e^{-i\omega t}dt$$

$$H(\omega) = \int_{-\infty}^{+\infty} h(t)e^{-i\omega t}dt$$

$$K(\omega) = \int_{-\infty}^{+\infty} k(t)e^{-i\omega t}dt$$

$$O(\omega) = \int_{-\infty}^{+\infty} o(t)e^{-i\omega t}dt$$

where $\omega = 2\pi f$ is the angular frequency and f is the classical frequency.
Because of the convolution theorem, the output signal can be written in the frequency domain as:

$$O_h = K(\omega)H(\omega) \qquad (3.10)$$

and hence:

$$o_h(t) = \frac{1}{2\pi} \int_{-\infty}^{+\infty} H(\omega)K(\omega)e^{i\omega t}d\omega \qquad (3.11)$$

The noise is a stochastic variable and stochastic processes are generally not Fourier-transformable. To understand the behaviour of noise, we first introduce the autocorrelation function, defined for a stationary process as:

$$R_{nn}(\tau) = E[n(t)n(t + \tau)]$$

that represents the extent of the statistical relationship between the process values at instants t_1 and t_2, and $t_2 = t_1 + \tau$; the operator $E[\cdot]$ indicates the expectetion

value. We can represent stochastic processes in the frequency domain using the *power spectral density (PSD)*, S_{nn}, which is related to the autocorrelation function by the Wiener- Khinchin's theorem:

$$S_{nn}(\omega) = \int_{-\infty}^{+\infty} R_{nn}(\tau)e^{-j\omega\tau}d\tau \tag{3.12}$$

The autocorrelation function of a process with zero mean, evaluated at $\tau = 0$, yields the variance:

$$\sigma_n^2 = R_{nn}(\tau = 0) = \frac{1}{2\pi} \int_{-\infty}^{+\infty} S_{nn}(\omega)d\omega \tag{3.13}$$

The noise power spectral density at the output of the filter S_n is related with that at the input S_{nn} through the equation [15]:

$$S_n(\omega) = |K(\omega)^2|S_{nn}(\omega) \tag{3.14}$$

The amplitude spectral density (ASD) is also used to analyse noise. The ASD is simply: $ASD = \sqrt{S_n(f)}$.

The expression of the signal-to-noise ratio is then obtained:

$$SNR \equiv \frac{|o_h(t)|^2}{\sigma_n^2} = \frac{1}{2\pi} \frac{|\int_{-\infty}^{+\infty} H(\omega)K(\omega)e^{i\omega t}d\omega|^2}{\int_{-\infty}^{+\infty} |K(\omega)^2|S_n(\omega)d\omega} \tag{3.15}$$

The matched filter is the linear filter that maximizes the SNR. Therefore the next step is to find the optimal $K(\omega)$ in order to maximize the SNR at a given time t_0 for the signal $h(t)$. For this purpose, we apply the Cauchy-Schwartz inequality:

$$|\int_{-\infty}^{+\infty} K(\omega)H(\omega)e^{i\omega t_0}d\omega|^2 \leq \int_{-\infty}^{+\infty} |K(\omega)|^2 S_n(\omega)d\omega \int_{-\infty}^{+\infty} \frac{|H(\omega)|^2}{S_n(\omega)}d\omega$$

and substituting into Eq (3.15), we obtain an upper bound for the SNR at the detection time t_0:

$$SNR \leq \frac{1}{2\pi} \int_{-\infty}^{+\infty} \frac{|H(\omega)|^2}{S_n(\omega)}d\omega \tag{3.16}$$

which is the optimal value of signal to noise ratio.

At the output of the interferometer the noise is made of differents contributions, such as shot noise, thermal noise and seismic noise plus several "technical" noises. Fig. (3.1) shows the amplitude spectral density (ASD) of the total strain noise in the LIGO-Hanford (red line), LIGO-Livingston (blue line) and Virgo (violet line) detectors. The curves represents the best performance of each detector during the run O3.
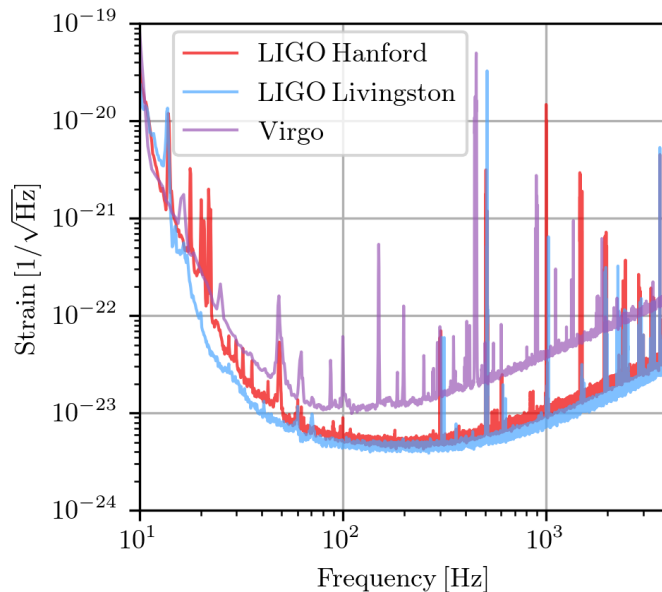
Figure 3.1. The plot shows frequency [Hz] on the x-axis, and the ASD value $[1/\sqrt{(Hz)}]$ on the y-axis. The data are not calibrated below 10 Hz and above 5 kHz. [7]

The above equations are general and independent of the form of $H(\omega)$. In the case of chirp signals the definition of Fourier transform of a chirp signal is given by Eqs. (1.44) (1.45). After averaging over source position and the inclination of he orbital plane, the computation of the SNR leads to:

$$SNR = \frac{2\sqrt{5}}{5\sqrt{6}} \left(\frac{GM_c}{c^3}\right)^{5/6} \frac{c}{\pi^{2/3}d} \sqrt{\int_{f_0}^{f_{ISCO}} \frac{f^{-7/3}}{S_n(f)} df} \qquad (3.17)$$

where d is the distance, f_0 is the signal frequency at the time t_0 and f_{ISCO} is defined in Eq. (1.50).

In practice, especially for low mass systems like those we are considering, f_{ISCO} can be much bigger than the maximum frequency accessible to current detectors, that is $f = 8192$ Hz. For instance, for a chirp mass of $M_c = 10^{-3} M_\odot$, the frequency at ISCO is $f_{ISCO} \simeq 1.5 \times 10^6$ Hz. Because of this, it is reasonable to replace the upper extreme of integration in Eq. (3.17) with f_{max} taken as the minimum between $f = 8192$ Hz and the frequency reached by the signal after an observation time of one year.

The plot in Fig. (3.2) shows the frequency evolution for a signal emitted by a source with chirp mass of $M_c = 10^{-3} M_\odot$ and an initial frequency of $f_0 = 20$ Hz. As we can see, the frequency of the signal evolves very slowly for a time of the order of months up to about $f = 100$ Hz, and then it rapidly increases until the coalescence. This is because the evolution of the signal is very fast in the last cycles and the two black bodies spend most of time in the inspiral phase.
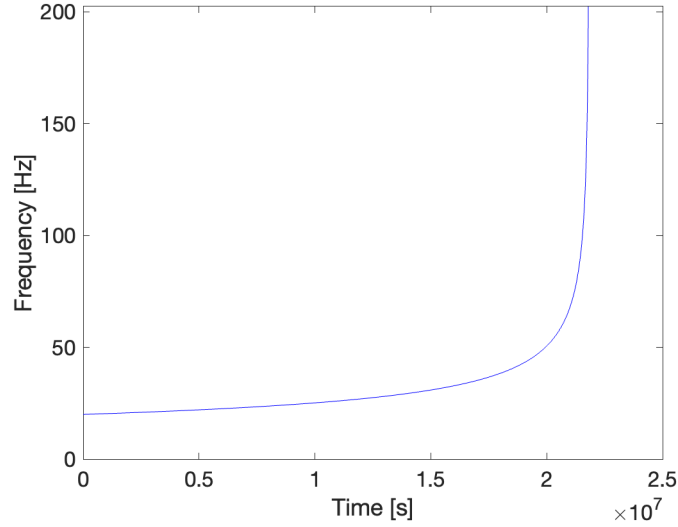
Figure 3.2. The plot represents the frequency evolution as a function of time for a chirp signal with chirp mass $Mc = 10^{-3} M_\odot$ and initial frequency of $f_0 = 20 Hz$. The evolution is very slow for about 8 months, later it proceeds very rapidly until the coalescence.

Taking into account this consideration for the evolution of the signal, we have studied the fraction of SNR that is accumulated as a function of a cut-off frequency, $f_{cut-off}$. This has been done by computing the ratio among the maximum SNR, obtained by Eq. (3.17) with upper extreme f_{max}, and the SNR corresponding to an upper extreme $f_{cut-off}$, which means estimating the following quantity:

$$\sqrt{\frac{\int_{f_0}^{f_{max}} \frac{f^{-7/3}}{S_n(f)} df}{\int_{f_0}^{f_{cut-off}} \frac{f^{-7/3}}{S_n(f)} df}}$$

Fig. (3.3) shows the SNR ratio as a function of the cut-off frequency $f_{cut-off}$ for $f_0 = 20$ Hz and source mass of $M_c = 10^{-3} M_\odot$.
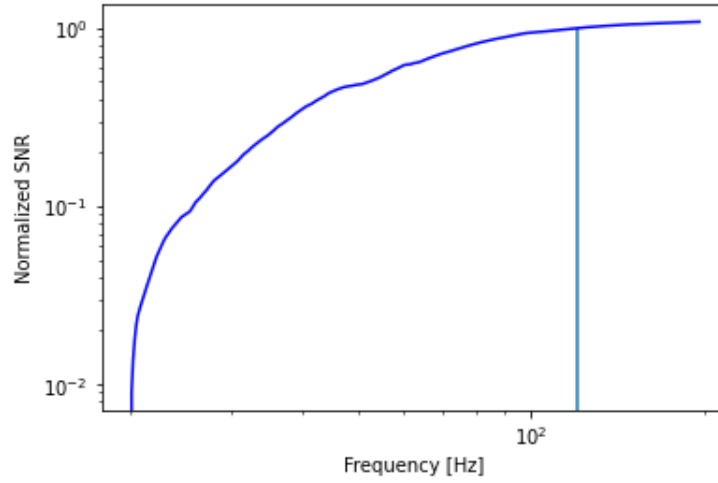
Figure 3.3. This plot shows the ratio of the SNR computed at f_{max} and $f_{cut-off}$ (see text for more details) as a function of frequency. The vertical line represents the cut-off frequency of 120 Hz. To estimate the SNR, the noise power spectral density of Virgo detector (03) has been used.

With this choice we see that taking $f_{cut-off} = 120$ Hz, i.e. focusing in the range $f \in [20, 120]$ Hz, about 90% of the SNR is still preserved.
For smaller masses, the evolution is slower and, in the case where the signal does not reach the cut-off frequency in one year of observation, there is no loss in terms of SNR.

Fig. (3.4) shows the minimum among the time to reach a cut-off frequency of 120 Hz and one year, as a function of the starting frequency f_0 and chirp mass M_c. The choice of this parameter space will be explained below, see Sec. (4.5.1). As we can see, for a significant portion of the parameter space the signal remains at frequencies below our cut-off, so its duration coincides with the total observation time (dark red region) and in this case there is no loss in terms of SNR. For the portion of parameter space corresponding to higher chirp masses and higher initial frequencies, the time required to reach the cut-off frequencies is shorter than the observation time and can be ∼ 5 days in the upper right corner of the frequency-chirp mass plane.
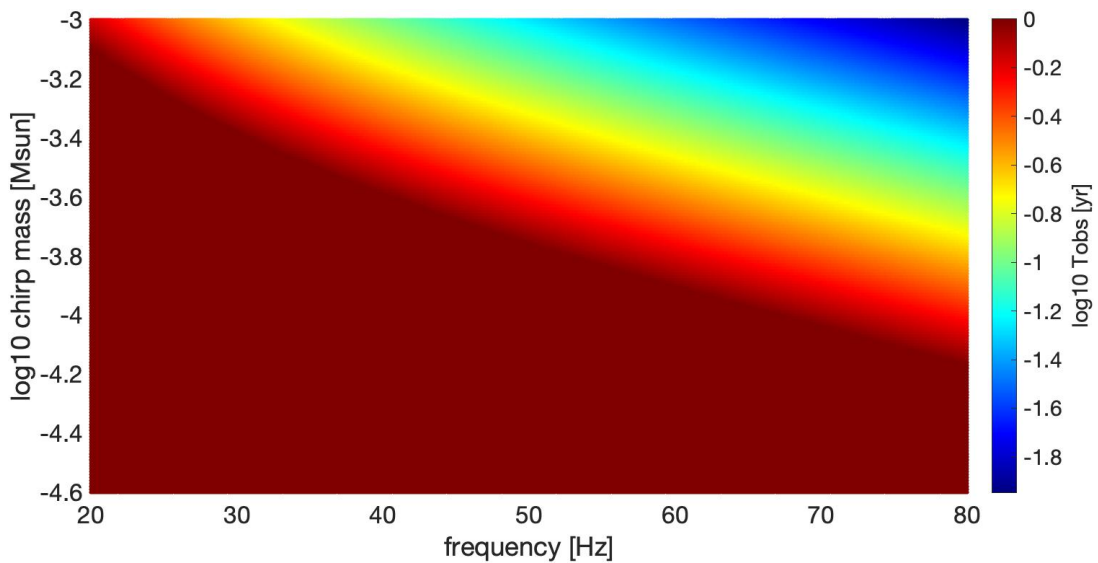
Figure 3.4. The figure shows the minimum between the time required for the signal to reach a cut-off frequency of 120 Hz and an observation time of one year, as a function of the starting frequency f_0 and chirp mass M_c. For most of the parameter space, the signal duration coincides with the total observation time (dark red region), while for high frequencies and large chirp masses (blue region) the signal duration is much shorter than the observation time.

The conclusion of this study is that we can limit the search for signals from PBHs to frequencies in the range $f \in [20, 120]$ Hz. This choice significantly reduces the computational cost of the analysis and, at the same time, makes the validity of the quadrupole approximation more robust.

Chapter 4

Data Analysis Method

The goal of this thesis is to develop a new data analysis method capable to increase the sensitivity of the search of GW from sub-solar mass PBH binaries in comparison to other methods that have been recently proposed [38]. Note that, we focus on masses smaller than those typically covered by LVK searches, as [9].
To increase the sensitivity naturally involves a higher computational cost.
The study of SNR introduced in the chapter allows us to reduce the computational cost by focusing the analysis on signal initial frequencies below a cut-off of $O(100Hz)$. In addition we focus attention on directed searches, pointing to a specific sky location like the galactic center.
In this chapter, which represents the core of the thesis, we will discuss the main data analysis technique used for building our pipeline, the construction of a grid in the parameter space, examples of application of the developed pipeline and a sensitivity estimation.

4.1 Types of searches

As previously mentioned, the idea is to perform continuous wave-like searches for inspiraling PBHs.
The searches for continuous wave signals or continuous wave signals are divided into three main categories:

- *target searches*: the relevant parameters of the systems, such as the signal frequency evolutions and sky position are known; in these searches we can correct exactly the phase evolution of the signal by knowing its sky location and frequency evolution;

- *directed searches*: only the position of the source in the sky is assumed to be known;

- *All-sky (blind) searches*: there is no knowledge of the source parameters.

The search sensitivity, i.e. the minimum detectable signal strain, depends on the observational time, but also on the balance between computational cost of the data analysis and computational resources. Target searches are computationally the easiest to perform. Since , the target search has the best sensitivity compared to

other classes but is limited to known sources. The most computationally intensive searches are all-sky searches that require well-optimised and robust algorithms, because the less is known about the source, the smaller sensitivity of the search can be reached and for a fixed amount of computational resources bigger computational cost is required. There are of course intermediate cases among the main three just discussed. All types of searches are summarised in Fig. (4.1).
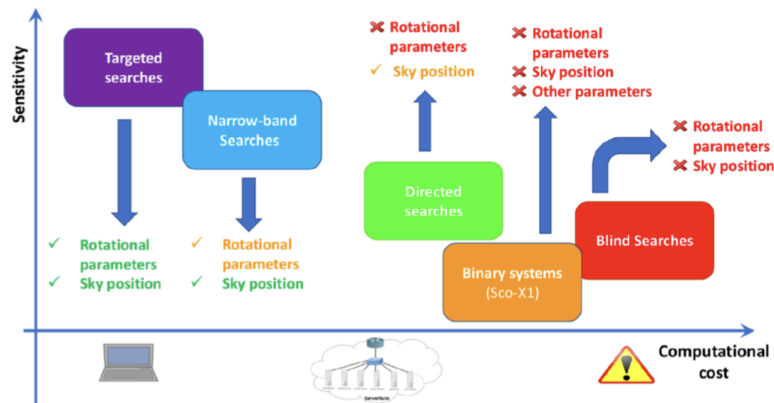

Figure 4.1. The figure shows sensistivity vs computational cost of several search strategies: more amore the unknown parameters, the higer is the computational cost.

For PBH binaries we do not know a priori the masses of the two components nor the emission frequency at a given time and there are no electromagnetic observations to give us such information; so, target searches are not possible. All sky searches would be plausible because, in principle, PBHs could be inspiraling anywhere in the sky. The method described in [38] proposes an all-sky methodology, but at the cost of a rather limited sensitivity. Since the goal of this thesis is to boost the sensitivity, we consider the directed search for PBHs pointing towards a known location, e.g. the Galactic Center, where we expect a high concentration of primordial black holes. For a fixed sky direction we search over a range of reference frequencies and chirp masses of PBHs binaries and this is more computationally feasible than all-sky searches.

4.2   Signal Model: 5-vector

To detect GW using LIGO-Virgo data, we need the analytical model to describe the GW strain induced in the interferometer.
Considering the reference frame of the detector, the strain signal in the time domain can be described as a linear superposition of the $+$ and $\times$ polarizations of the GW according to the detector's response [2]

$$h(t) = h_+(t)F_+(t; \Psi) + h_\times(t)F_\times(t; \Psi) \tag{4.1}$$

where F_+ and $F_\times$ are the two beam-pattern functions.

For a continuous GW signal, the expected strain at the detector is [14]

$$h(t) = H_0(A_+ H_+ + A_\times H_\times)e^{j(\omega_0(t)t+\gamma)} \tag{4.2}$$

where $\frac{\omega_0(t_0)}{2\pi} = f_0$; the *plus* and *cross* amplitudes are given by

$$H_+ = \frac{\cos 2(\Psi) - j\eta \sin(2\Psi)}{\sqrt{1+\eta^2}}$$

$$H_\times = \frac{\sin(2\Psi) + j\eta \cos(2\Psi)}{\sqrt{1+\eta^2}}$$

in which η is the ratio of the polarization ellipse semi-minor to semi-major axis and Ψ is the polarization angle that defines the direction of the major axis with respect to the celestial parallel of the source (counter-clockwise). The parameter η is within the range $[-1, 1]$, where $\eta = 0$ for a linearly polarized wave and $\eta = \pm 1$ for a circularly polarized wave. The two complex amplitudes satisfy the condition $|H_+|^2 + |H_\times|^2 = 1$. The functions $A^+(t)$ and $A^\times(t)$ describe the detector response as a function of time and are equivalent to the beam functions in Eq. (4.1), computed for $\Psi = 0$. These functions depend on the source position, the detector location, orientation and sideral motion.

The effect of detector response on a monochromatic signal is to introduce an amplitude and phase modulation which determines a split of the signal power into five frequencies: ω_0, $\omega_0 \pm \Omega$, $\omega_0 \pm 2\Omega$, where ω_0 is the intrinsic angular frequency of the signal and Ω is the Earth's sidereal frequency. This model is also known as "5-vector" and is caused by the Earth sidereal motion.

Due to the Earth's motion, the signal is also subject to the Doppler effects. For this reason, the instantaneous value of the observed frequency f changes over time and the signal arrives at the detector with a frequency modulation. The emitted frequency $f_0(t)$ and the frequency of the signal at the detector $f(t)$ are related by [13]

$$f(t) = \frac{1}{2\pi}\frac{d\phi(t)}{dt} = f_0(t)\left(1 + \frac{\vec{v}\cdot\hat{n}}{c}\right) \tag{4.3}$$

where $\vec{v} = \vec{v}_{orb} + \vec{v}_{rot}$ is the detector's velocity with respect to the *Solar System Barycentric* (SSB) reference frame, given by the sum of the Earth's orbital and rotational velocity, and $\hat{n}$ identifies the source position in the (SSB).

Furthermore, we have to take into account that the intrinsic frequency of the emitted signal increases in time according to Eq. (1.40) and this contributes to frequency modulation as a *spin-up* effect according to Eq. (1.37).

4.3   Band Sampled Data

In this thesis, the Band Sampled Data (BSD) framework [41] is employed to develop a method for the directed search for primordial black hole binaries.
The BSD framework allows to easily combine dataset according to a specific purpose and to optimise the choice of parameters to be used in a given search. This flexibility translates directly into increase the possibility to write computationally efficient codes which, on its turn, implies an increase of sensitivity at fixed computing cost.

The construction of the BSD database starts from a collection of overlapped short Fourier Transforms (FFTs), called "Short FFT Data Base" (SFDB) [12], used for many all-sky CW analysis in the Virgo collaboration.

- From the SFDB files a band of 10 Hz is extracted

- The Inverse Fourier Transform (IFFT) is calculated and are subsampled to the inverse of the bandwidth, i.e. $\frac{1}{\Delta f_{BSD}}$ s

- Creation of the *reduced-analytic signal*

- Since FFTs are half-interlaced, the first and last quarters of the time-domain data are eliminated, conserving the central part.

- these chunks of data are stored in the BSD file

N-FFTs covering 1 month's data are considered and this procedure is applied; then we move on to the next 10 Hz band. In conclusion, we get a set of data blocks of size '10 Hz/1 month', which is the BSD database.
The time domain data are stored in the so-called reduced analytical signal format, as mentioned in the third point, that is different from the classical analytical signal. In the original SFDB, only the positive part of each FFT is stored, so the classical analytical signal requires zeros to be added to the FFT before performing the IFFT, being sampled at $f = 2f_{max}$, as required by Nyquist's theorem. The reduced analytical signal is a complex time series with only positive frequency but is obtained by discarding the negative and zero component of the classical analytical signal sampled at $f = f_{max}$ [42].
The Fig. (4.2) illustrates the steps of BSD construction, and Fig. (4.3) shows the resulting BSD database.
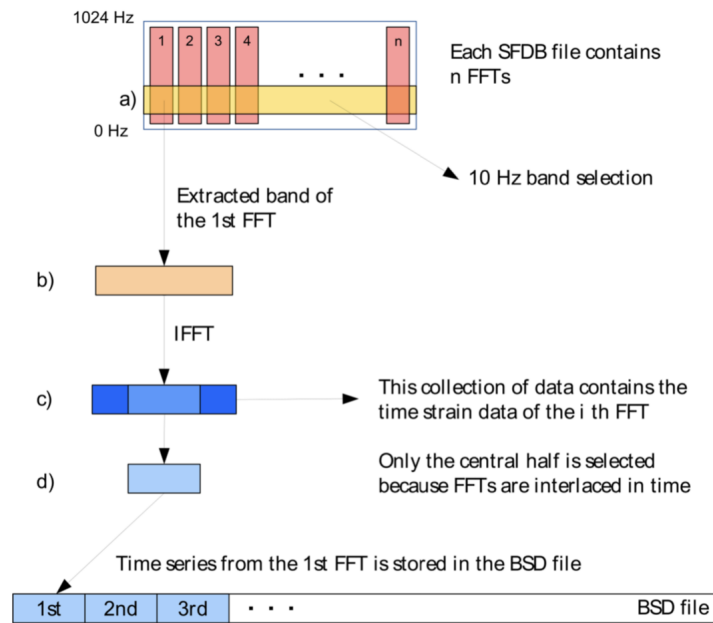
Figure 4.2. The different steps leading to a single '10 Hz/1 month' block. (a)-(b) the frequency length in Hz is chosen and extracted (for example 10 Hz); (c) IFFFT is performed on this i−th FFT and (d) only the central part is taken. The resulting analytical signal is a single piece of the BSD file that will be filled with all n-FFTs of the selected 10 Hz band. [42]
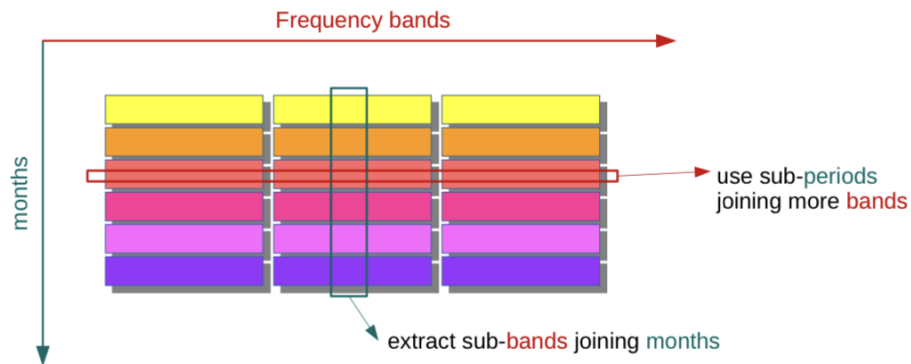

Figure 4.3. Illustration of extraction of a sub-bands from the blocks, that can be performed respect to frequency or time direction

The great advantage of BSD is that are flexible data structures easy to handle: they are in time domain rather than frequency domain and the data chunk duration, called *coherence time* T_{FFT}, is not fixed but it is possible to create a set of FFTs with a duration optimized for the search.

4.4   Heterodyne Correction

In section (4.2) we introduced that the continuous GW signal has a frequency modulation due to the intrinsic spin-up and the Doppler effect. A key concept in the search for CW is the removal of any frequency modulation, so that the demodulated signal becomes monochromatic. In this situation, its frequency content would be confined into a single frequency bin, thus increasing its detectability. A technique used to demodulate the signal is based on the heterodyne procedure.

The *heterodyne correction* consists in multiplying the data by a complex exponential function that removes the phase modulation. Assuming to know the signal parameters which affect the phase, the corrected data has the form

$$y(t) = [h(t) + n(t)]e^{-i\phi_{corr}(t)} \tag{4.4}$$

where $\phi_{corr}(t)$ is the total phase correction

$$\phi_{corr}(t) = \phi_{su}(t) + \phi_d(t) \tag{4.5}$$

given by the contribution of the phase shift due to the source spin-up ϕ_{su}

$$\phi_{su}(t) = \int_{t_0}^{t} 2\pi f_{gw}(t')dt' \tag{4.6}$$

and ϕ_d, the phase shift due to the Doppler effect, which can be written as:

$$\phi_d(t) = 2\pi \int_{t_0}^{t} f_{gw}(t')\frac{\vec{v} \cdot \vec{n}}{c}dt' \simeq \frac{2\pi}{c}p_{\hat{n}}(t)f_0(t) \tag{4.7}$$

where $p_{\hat{n}(t)}$ is the position of the detector in the chosen reference time, projected along the source sky position $\hat{n}$. After heterodyne correction the signal should appear monochromatic, apart from some residual modulations, $\delta\Phi = \Phi(t) + \Phi_0 - \Phi_{corr}(t)$ which haven't been taken into account (e.g. due to the uncertain knowledge of the parameters) and there is still a modulation due to the non uniform antenna pattern, which spread the signal power at five frequencies, as said in Sec. (4.2). From a practical point of view, the sidereal modulation affects the analysis only if the frequency resolution is smaller than the signal spread, i.e. if the data segment duration T_{FFT} is larger than about one sidereal day, see Sec. (4.5).

4.4.1   Peakmaps

The method presented here is based also on some other well established concepts and procedures for CW search, such as the use of the peakmaps, used in the context of the BSD framework. [35]

A peakmap is defined as a collection of the most significant peaks in the time$-$frequency plane. After splitting the data in segments of duration T_{FFT}, see Sec. (4.5), to select a peak (defined as local maxima above a given threshold) the following ratio have to be calculated:

$$\mathcal{R}(i,j) = \frac{S_{P;i}(f)}{S_{AR;i}(f)} \tag{4.8}$$

where $S_{P;i}(f)$ is the periodogram, i.e. the square modulus of the FFT computed over the $i-th$ data segment and $S_{AR;i}(f)$ is an auto$-$regressive average spectrum estimation over the same time interval (Fig. 4.4(a)). This ratio is computed for each $j-th$ frequency bin of a given FFT.

For each pair (i,j), are selected the elements of $\mathcal{R}(i,j)$ for which are valid both the conditions:

- $\mathcal{R}_{ij}$ is above a threshold θ_{thr}

- is a local maximum with respect to its $(j-1, j+1)$ neighbouring bins

Every time this occurs, the corresponding peak is selected and the surviving bin contributes to the peakmap. The choice of threshold θ_{thr} is critical because affects the sensitivity of the search and its computational weight, while the addition of the local maximum condition gives the criterion greater robustness against disturbances. An example of the ratio $\mathcal{R}$ and the selection of local maxima peaks above the threshold in shown in Fig. (4.9(b)).
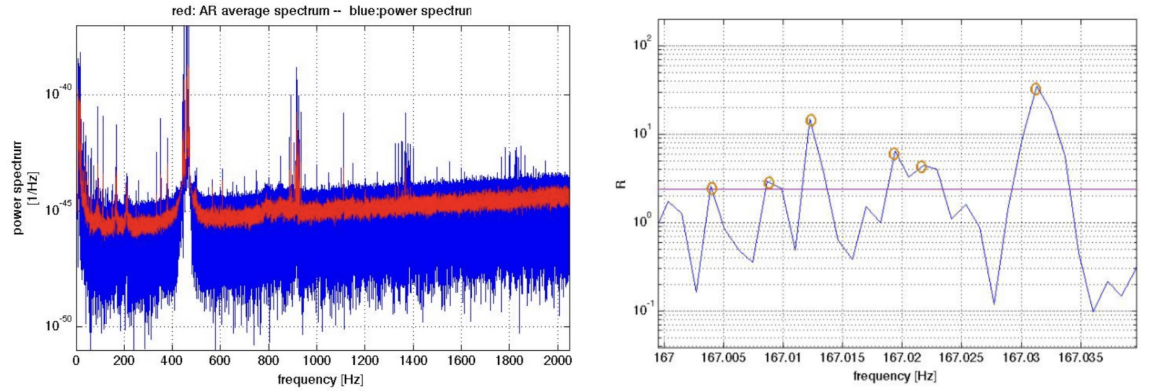
(a) Illustration of the spectrum (blue) and mean spectrum (red) of VSR4 data (Virgo detector)

(b) Zoom on the ratio R in a small frequency band from the VSR4 data. The horizontal line stands for the threshold θ_{thr} while the orange circles are the peaks, that are also local maxima, which will then be selected to create the peak map.

Figure 4.4

It is important to assess how many signal peaks may be missed and how many noise disturbances are selected in the peak map, because both impact the analysis. Assuming gaussian noise, the probability to select a peak due to the *noise* is $P(\theta; 0) = p_0$ and has the form of

$$p_0 = \int_{\theta}^{+\infty} e^{-x}(1 - e^{-x})^2 dx = e^{-\theta} - e^{-2\theta} + \frac{1}{3}e^{-3\theta}$$

where $e^{-x}dx$ is the probability of having a value of $R(i,j)$ in $[x; x+dx]$ and $(1-e^{-x})^2$ that this value is also a local maximum. If there is a signal with spectral amplitude

λ, the probability to select a signal peak is

$$p_\lambda \approx p_0 + \frac{\lambda}{2}\theta(e^{-\theta} - e^{-2\theta} + \frac{1}{3}e^{-3\theta})$$

The probability of having n peaks in the Peakmap is binomial with $\mu = N_{tot}p_0$ and $\sigma = \sqrt{N_{tot}p_0(1-p_0)}$, where N_{tot} is the total number of bins in the Peakmap. With a sufficient high number of T_{FFT}s, i.e. N, the binomial distribution can be approximated to a Gaussian one [12].

The detection statistic is determined by the *critical ratio CR*:

$$CR = \frac{n - Np_0}{\sqrt{N}p_0(1 - p_0)} \qquad (4.9)$$

The value of θ_{thr} can be obtained by maximising the expectation value of the critical ratio:

$$\mu_{CR}(\theta, \lambda) = \frac{N(p_\lambda - p_0)}{\sqrt{N}p_0(1 - p_0)}$$

It turns out that the choice of $\theta_{thr} = 2.5$ is a reasonable value that produces only a small loss in sensitivity of the search, and the local maximum condition prevents the selection of disturbances in the data because they are distributed over more than one bin.

4.5   Method description

In this section we will describe in detail the analysis method developed for the search of signals emitted by sub-solar mass PBHs. The procedure exploits the concepts and tools described in the previous sections.

Our approach is based on a semi-coherent hierarchical search method, where an heterodyne correction over a "coarse" grid in the parameter space is followed by a "refined" correction in which the information on the signal phase is not used, see the scheme in Fig. (4.5). In this search, we can break down the observation time into many chunks and combine their information. We assume that we know the position but have no information about the value of the parameters that determine the phase evolution.
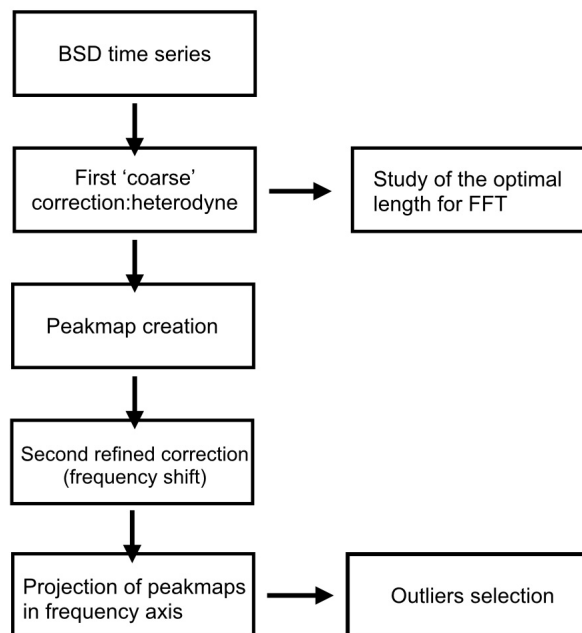
Figure 4.5. Scheme of the semi-coherent approach applied to the acquired data.

Let us examine more in detail the various steps illustrated in this diagram.
We consider a black hole binary emitting at an unknown initial frequency f_0, with unknown chirp mass M_c and known sky position (λ, β).
The analysis begins from the calibrated data time series produced in the BSD framework [41].
The first step consists in performing coarse Doppler and spin-up correction using the heterodyne procedure according to Eq. (4.7). The coarse correction is done on a grid in the parameter space (f_0, M_c), determined as described in the following section (4.5.1) and (4.5.2). Once the coarse correction has been done, the time-frequency

peakmap is built and, on this, a refined correction is applied by properly shifting the frequency of the peaks, as described in section (4.5.3). Finally, the peakmap is projected on the frequency axis and outliers are selected. Further steps, not discussed in this thesis, concern the coincidences among outliers found in different datasets (e.g. produced by different detectors), and the follow-up of the most significant candidates.

4.5.1   Coarse grid in the parameter space

For a given sky position, a coarse grid in the parameter space consisting on an initial frequency and chirp mass, (f_0, M_c) is built.

In section (3.1) we proved the validity of the quadruple approximation, which allows the parameter space to be reduced to f_0, M_c, t_0 and ι. The inclination angle ι is not involved in the signal phase and then can be neglected for the moment. Regarding the initial time parameter t_0, let us make the following consideration: we do not know the initial time instant at which the gravitational signal originates nor the signal frequency at the reference time t_0 (corresponding, for instance, to the initial time of the data). However, we can say that a signal corresponding to time $t' = (t_0 \pm Dt)$ can be seen as entering the sensitivity band of the interferometer at an initial frequency f_0' lower or higher than f_0; it is therefore possible to include the dependence of the problem on the initial time into the dependence on the initial frequency. This means that we can further reduce the parameter space to one that depends only on the initial frequency and chirp mass.
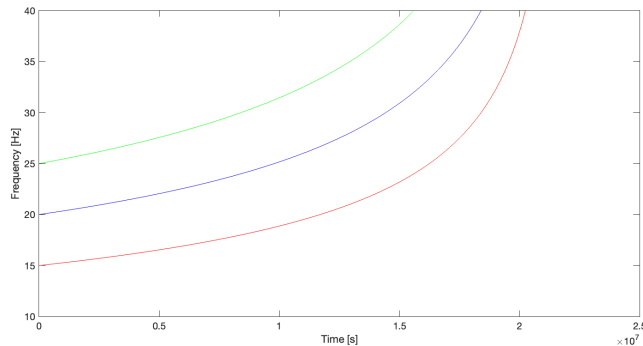
Figure 4.6. Plot of the frequency evolution of three signals starting at different initial frequencies $f_0 \pm Df$.

Here we select a range for the possible initial frequencies $f_0 \in [20, 80]$ Hz: $f_{0,min} = 20$ Hz represents the minimum frequency of the detector bandwidth sensitivity, while $f_{0,max} = 80$ Hz is an arbitrarily chosen value, such that, for most of the considered parameter space, the signal frequency at the end of the observation time, assumed here to be of one year, is below the cut-off frequency $f_{cut-off} = 120$ Hz, see Sec. (3.2). As for the chirp masses, we explore a range of $M_c \in [10^{-4.6}, 10^{-3}]$ $M_\odot$. The lower value of the chirp mass corresponds to an initial spin-up comparable to the maximum spin-up covered by standard CW searches. [8]

The grid is then computed as a compromise between sensitivity and computational

cost. Of course, the smaller the chosen step, the denser the grid will be and the better the sensitivity, i.e. smaller mismatch among signal and template, but on the other hand the greater the computational cost will be. For example, by taking a frequency step of $Df_0 = 0.01$ Hz and chirp mass step of $DM_c = 10^{-6} M_\odot$, there are about 6 million points in the parameter space (see next section). As will be explained in the next section, the steps (Df_0, DM_c) determine the maximum duration of the data segment within which the residual frequency variation, due to a mismatch between the actual signal frequency and the assumed frequency evolution, is contained into a frequency bin. This is the duration of the data segments which will be used in the subsequent time-frequency analysis, referring to the construction of the peakmap in Scheme (4.5).

4.5.2 Computation of the optimal data segment duration

In the analysis scheme described in the previous section, the computation of a maximum duration for data segmentation will then have an impact in the creation of the peakmaps (time/frequency map), described in section 4.4.1. The chunk duration, T_{FFT}, is called *coherence time.* In order to study the optimal coherence time, the request is that, in the time interval given by the data segmentation duration, the residual of frequency variation between two signals with parameters (f_0, M_c) and with parameters $(f_0 + Df_0, M_c + DM_c)$,after having corrected for the pair (f_0, M_c), remains confined into one frequency bin.

In order to compute the optimal T_{FFT}, we consider two trajectories in the time-frequency plane, one of which originates at the point (f_0, M_c), and the other at an adjacent grid point, (f'_0, M'_c), where $f'_0 = f_0 + Df_0$ and $M'_c = M_c + DM_c$.
Since the gravitational signals considered here are very long in time, the frequency evolution will be calculated up to a time equal to the minimum value between the time required for the signal to reach the cutoff frequency $f_{max} = 120$ Hz, and the observation time, which we denote as T_{obs} and which, in explicit computations, we will take equal to one year.
For clarity, let us rewrite the frequency evolution for the two signals starting at two adjacent points in the parameter space, after a time of T_{obs}:

$$f(t) = f_0 \left[1 - \frac{8}{3} K f_0^{8/3} T_{obs} \right]^{-\frac{3}{8}} \tag{4.10}$$

$$f'(t) = (f_0 + Df_0) \left[1 - \frac{8}{3} K'(f_0 + Df_0)^{8/3} T_{obs} \right]^{-\frac{3}{8}} \tag{4.11}$$

where:

$$K \equiv \frac{96}{5} \pi^{\frac{8}{3}} \left(\frac{GM_c}{c^3} \right)^{5/3}$$

$$K' \equiv \frac{96}{5} \pi^{\frac{8}{3}} \left(\frac{G(M_c + DM_c)}{c^3} \right)^{5/3}$$

and the frequency variation as a function of time is given by

$$\Delta f = |f'(t) - f(t)| \tag{4.12}$$

At this point, we compute the quantity (4.12) at two arbitrary times t_1 and t_2 and then we estimate their difference: $\Delta f(t_1) - \Delta f(t_2)$.
The criterion that the entire power signal is contained in a single bin is satisfied by ensuring the following condition:

$$|\Delta f(t_1) - \Delta f(t_2)|_{max} \leq \frac{1}{|t_1 - t_2|} \tag{4.13}$$

where we take the maximum difference across the whole observation time T_{obs}.
The corresponding time difference $|t_1 - t_2|$ defines the optimal T_{FFT}. The frequency bin is given by the inverse of the coherence time

$$\delta f = \frac{1}{T_{FFT}}$$

Such T_{FFT} will be used in the subsequent step of the analysis to build the time-frequency peakmap, as described in previous section, is based on the computation of of FFTs of data segments of duration T_{FFT}.

Since the frequency difference between the two trajectories of the frequency evolution increases with time, we are sure to take the maximum value of the difference in Eq.(4.13) at two instants of times $t_1 = T_{obs} - Dt$ and $t_2 = T_{obs}$ in a time interval between T_{obs} and an adjacent time $(T_{obs} - Dt)$.
Thus we have:

$$
f(T_{obs}) - f'(T_{obs}) = f_0 \left[1 - \frac{8}{3} K f_0^{8/3} T_{obs} \right]^{-\frac{3}{8}} + \\
- (f_0 + Df_0) \left[1 - \frac{8}{3} K'(f_0 + Df_0)^{8/3} T_{obs} \right]^{-\frac{3}{8}}
\tag{4.14}
$$

and

$$
f(T_{obs} - Dt) - f'(T_{obs} - Dt) = f_0 \left[1 - \frac{8}{3} K f_0^{8/3} (T_{obs} - Dt) \right]^{-\frac{3}{8}} + \\
- (f_0 + Df_0) \left[1 - \frac{8}{3} K'(f_0 + Df_0)^{8/3} (T_{obs} - Dt) \right]^{-\frac{3}{8}}
\tag{4.15}
$$

Finally, we have to subtract these last two equations to obtain the condition determining the maximum length for FFT duration.
The chosen coarse grid step will provide the T_{FFT} according to Eq. (4.13).

In Fig. (4.7), the colorbar shows the values of T_{FFT} as function of the frequency and of the chirp mass in the parameter space, considering a time of observation of 1

year. Longer T_{FFT} are allowed at lower frequencies and smaller masses; on the other hand, as we will see later, the use of longer coherence times increases the search sensitivity but requires higher computing power. T_{FFT} ranges from approximately 100 at higher chirp masses and frequencies, to about 148000 s for lower masses and frequencies. We note that at higher f_0 there is a gradual transition from higher to lower values of T_{FFT}; in contrast, at smaller f_0 there is a much faster decrease. This is due to the specific dependence of the time-dependent signal frequency $f_{gw}(t)$ on the parameters (f_0, M_c).
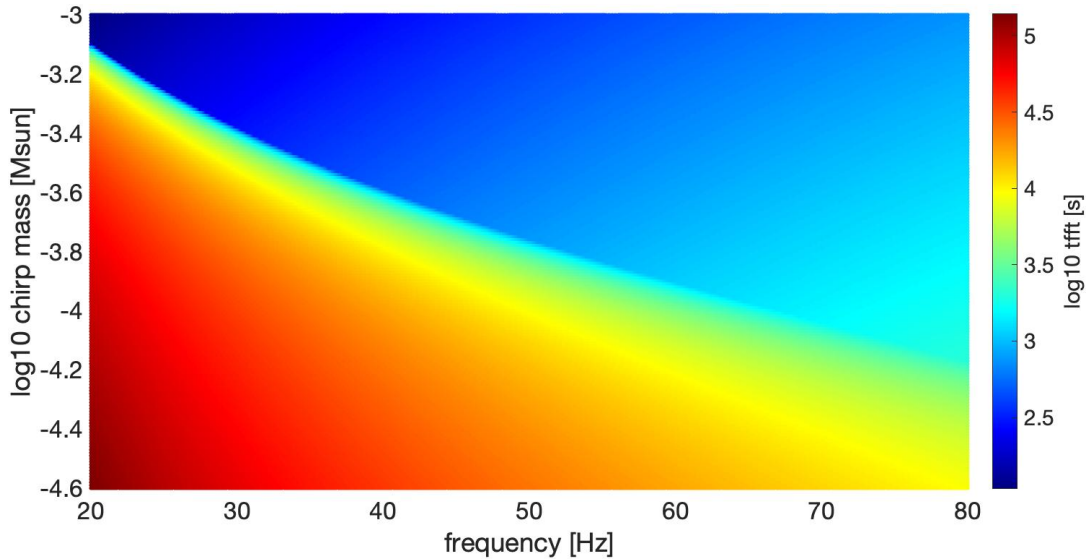
Figure 4.7. Maximum length duration of the FFT in seconds as a function of frequency and chirp mass. T_{FFT} ranges from about 100 s (blue section), corresponding to higher masses and frequencies, to 148000 s for lower masses and frequencies (red section).

The behaviour of T_{FFT} reflects in the behaviour of the initial spin-up value, $\dot{f}_0$, as shown in Fig. (4.8). Larger $T_{FFT}s$ correspond to smaller spin-ups and vice-versa. In particular, the parameter space (f_0, M_c) we are considering corresponds to spin-ups in the range between $\sim 10^{-9}$ and $\sim 10^{-4}$ Hz/s.
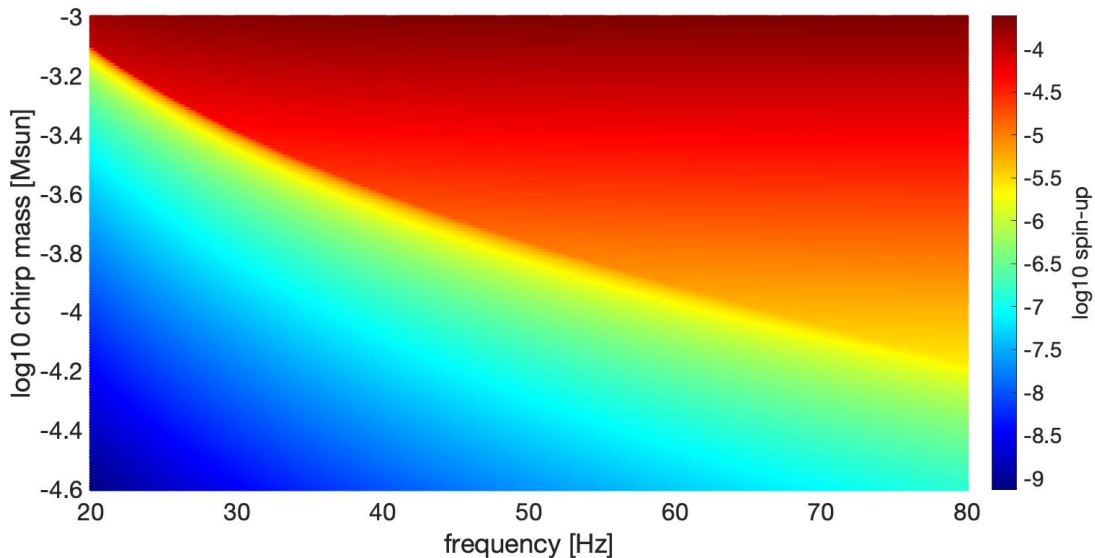
Figure 4.8. Spin-up as a function of frequency and chirp mass in the parameter space. The maximum spin-up is obtained for higher source masses and initial frequencies.

4.5.3 Peakmap creation and refined correction

The peakmaps are created starting from a given BSD covering 1 month and 10 Hz. If a strong signal is present in the data, it can be tracked in the peakmaps.
As explained in Sec. (4.2), BSD are flexible data structures developed to efficiently handle data. An important advantage of this database is the tuning of the coherence time T_{FFT}. In fact, we can change the T_{FFT} according to the search we perform and use the optimal coherence time found in Sec. (4.5.2). Using the optimal T_{FFT} provides a higher CR. This is extremely useful for signals with smaller amplitudes, because with too small T_{FFT} they might be difficult to identify, or might be missed in the analysis. Therefore, depending on the parameter space covered by the search, the optimal value of T_{FFT} is taken from Fig. (4.7) and with this value, the peakmap can be created. It is clear that a well-defined grid is required to ensure that the frequency shift is less than the frequency bin of the peakmap.

Following the scheme (4.5), the next step of the hierarchical procedure is to apply a second refined spin-up correction; this correction requires a shifting of the peaks. In this work, this step has not yet been implemented but it will be carried out in a future work.
Lastly, the peakmap can be projected on frequency axis and the outliers, that is the most significant peaks in the projection, are selected and subject to further analysis steps can be selected. Some examples of peakmaps, obtained after the injection of simulated signals in real data, are presented and discussed in the next section, which is devoted to a validation of the analysis procedure.

4.6   Test of the analysis method

In this section, we will show some tests for the simulated signals of two PBH inspirals injected into O3 real data. We then attempted to recover the injection using the method described in the previous section, in order to check the validity of the procedure.

For this purpose, we have used data from the third observing run (O3) of the Advanced LIGO detectors in Hanford (H) and Livingston (L). The analysis was carried out using the functions of SNAG (*Signal and Noise for Gravitational Antennas*), a software package for the detection of gravitational waves. SNAG software have been developed mainly to search for continuous GWs from isolated neutron stars, but contains many routines for more general data analysis tasks.

In this work, we have tailored various pre-existing codes to the case of a binary black hole system adding the proper phase evolution term for the Doppler and spin-up effect and reading the relevant parameters from a source structure like the following one:

```
function sour= PBH
    sour.f0=34.7;
    sour.luminosity_distance=10;
    sour.theta_jn=0.4;
    sour.chirpmass=5.0119e(-5);
    sour.bhbh=1;
    sour.a=hour2deg('17:45:40.0409');
    sour.d=-29.00781;
```

The software injection have been generated using the function `bsd_softinj_re_mod`, part of SNAG toolbox. We have extended this code to include the possibility to simulate the inspiral of PBH binary systems.

To run these tests, we worked with a BSD file covering 10 Hz and 1 month. Signals with different parameters have been simulated. In the following we report results for a specific simulation with parameters $f_0 = 33.4$ Hz and $M_c = 5.0119 \cdot 10^{-5} M_\odot$. As we are mainly interested in validating the analysis procedure, we have simulated signals with high strain amplitude, in the order of $h_0 \sim 10^{-20}$. The method sensitivity, connected to the minimum detectable strain, will be discussed in section (4.7).

The power spectrum of the simulated signal is displayed in Fig.(4.9) and, as we can see, it is affected by Doppler and spin-up modulation.

(a) .

(b) .
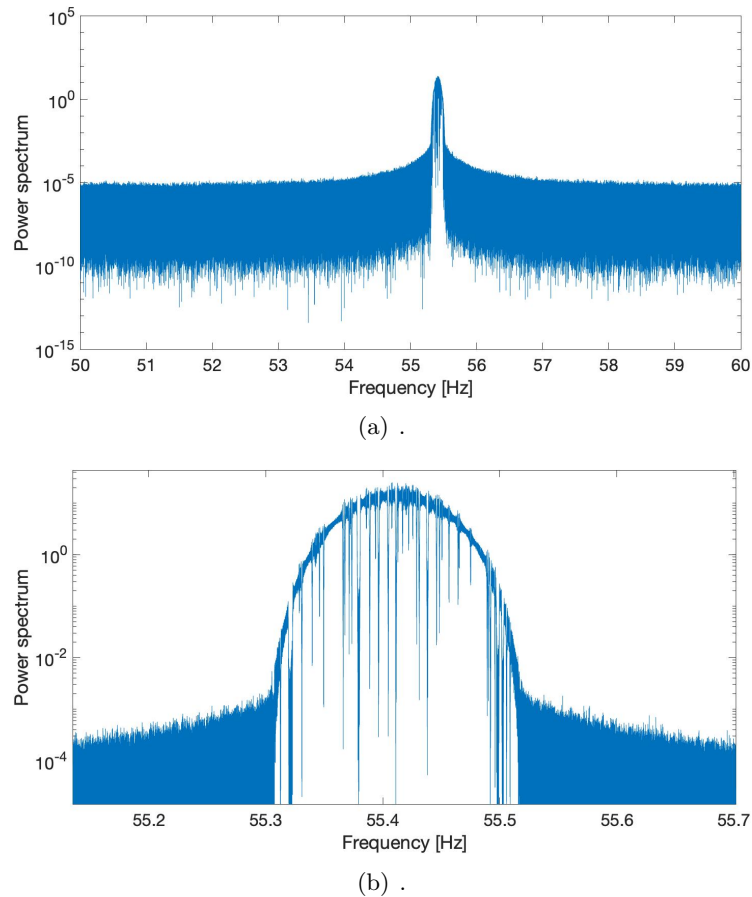
Figure 4.9. *Upper*: Power spectrum in units of 10^{-40} 1/Hz. The simulated signal is injected in Livingstone data (O3) with parameters of $f_0 = 33.4$ Hz and $M_c = 5.0119 \cdot 10^{-5} M_\odot$. *Bottom*: zoom of the upper plot .

As a first test, the heterodyne correction have been carried out -using the exact signal parameters- with the SNAG function `bsd_dopp_sd`. This function was also heavily modified as part of the thesis work to allow for spin-up correction for inspiralling PBH.

As shown in Fig. (4.10(b)), after removal of Doppler modulation and intrinsic signal spin-up, the signal power spectrum shows the effects of sidereal modulation in the form of five peaks at frequencies f_0, $f_0 \pm \Omega$, $f_0 \pm 2\Omega$ the typical shape of the five vectors is easily recognisable. The relative amplitude of the peaks depends on the position and polarization parameters of the source and the modulation is given by the response of the detector.

(a) .

(b) .
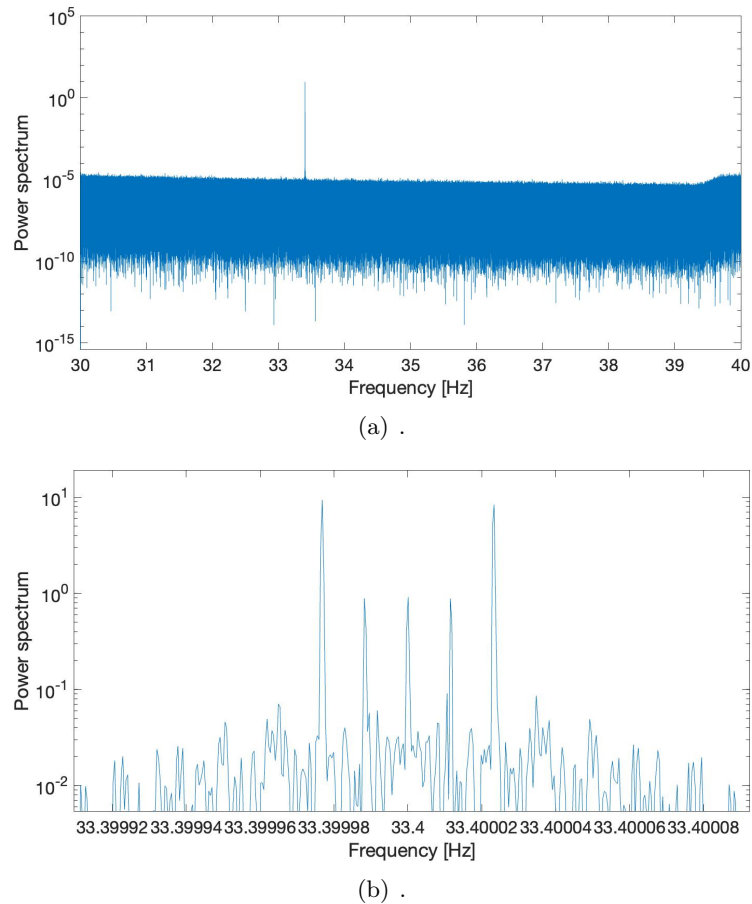
Figure 4.10. *Upper*: Power spectrum of the injected signal after the application of heterodyne. *Bottom*: the plot is a zoom around the frequency of the injection. The signal shows the typical split due to the sideral motion of the detector.

In real cases, the signal parameters are not known exactly, so a grid is constructed in the plane (f_0, M_c), as discussed in Section (4.5.1). For each grid point, a heterodyne correction is applied to the entire data set, which should partially correct for Doppler modulation and intrinsic spin-up of the signal.

We then performed some tests to verify this aspect. Specifically, I wrote a code to inject a signal with specific parameters (f_0, M_c) into the real data and then created a narrow grid around these values; the heterodyne correction was applied only to this small grid, to save on computational costs.

Before, since the observation time covered by the data is 30 days, we again evaluate the optimal length of the FFT in this case. Graph (4.11) shows the length of the FFT as a function of parameter space in the case of T_{obs}=1 month.
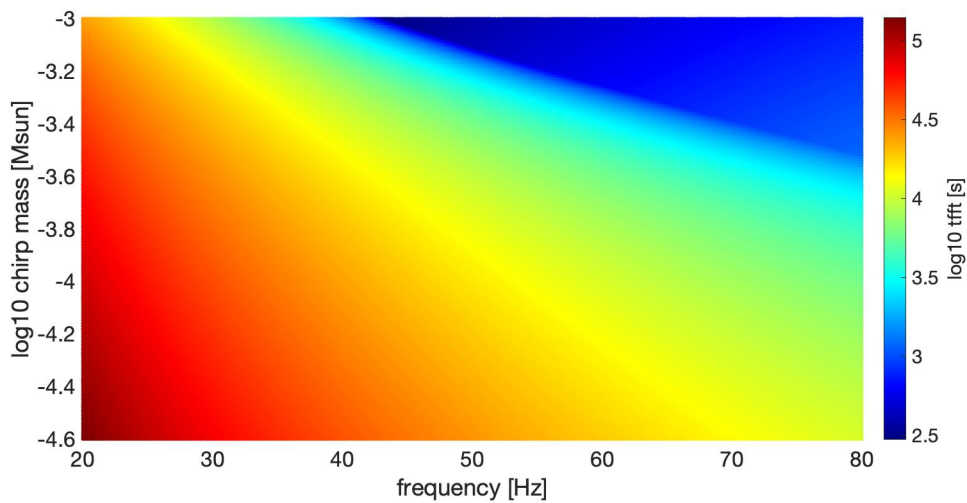
Figure 4.11. Maximum length duration of the FFT in seconds as a function of frequency and chirp mass for a T_{obs}=1 month.

For example, peakmaps have been created for Livingstone data covering the frequency band [50,60] Hz and [30, 40] Hz and an injected signal with parameters tabuled below:

f_0 [Hz]	M_c [$M_\odot$]	h_0	T_{FFT} [s]
55.3	$5.0119 \cdot 10^{-5}$	10^{-22}	17022
34.7	$2.5119 \cdot 10^{-4}$	10^{-22}	20750

A small grid was constructed around the signal in the frequency-chirp mass plane; an example is shown in Fig. (4.12) Here we show the case of an equidistant grid with a step of $Df_{grid} = 4 \times Df_0$ along the frequency axis and $DMc_{grid} = 4 \times DM_c$ along the mass axis of the chirp, with $Df_0 = 10^{-2}$ Hz and $DM_c = 10^{-6}$ $M_\odot$. However, further tests were carried out, also with grids with random coordinates, covering different sections of the parameter space, in order to check that the procedure worked properly.
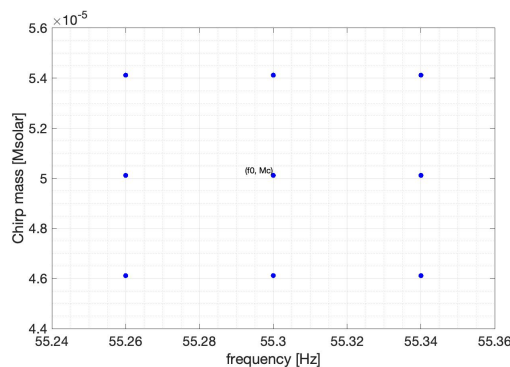
Figure 4.12. Example of a small test grid constructed around the point (f_0, M_c) in parameter space. The heterodyne correction is applied at each point of this grid.

To create the peakmaps we used a $T_{FFT} = 17022$ s for the signal with parameters $f_0 = 55.3$ Hz and $M_c = 5.0119 \cdot 10^{-5} M_\odot$; while for the signal with $f_0 = 34.7$ Hz and $M_c = 2.5119 \cdot 10^{-4} M_\odot$ we used a $T_{FFT} = 20750$. These values are determined by the T_{FFT} reported in the graph (4.11). The peakmaps are shown in Figs. (4.13) and (4.14): the color represents the critical ratio at each time in a particular frequency band. In both cases, we can recognise the track of the simulated signal from the inspiralling binary.

(a)

(b)
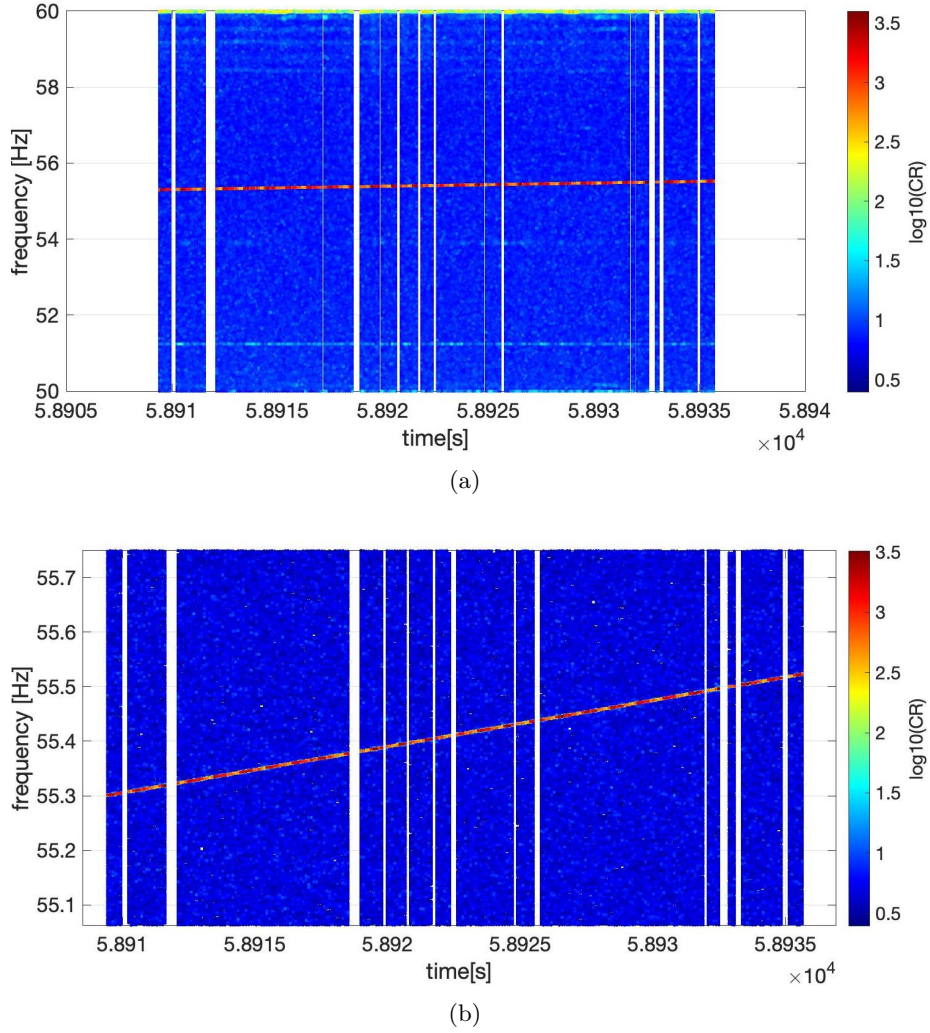
Figure 4.13. *Upper*: Peakmap created with a $T_{FFT} = 17022$ s of a signal after the injection of a signal with: $f_0 = 55.3$ Hz and $M_c = 5.0119 \cdot 10^{-5} M_\odot$. *Bottom*: a zoom of the peakmap on top around the frequency of the injection, where the effect of spin-up is clearly evident.

(a)

(b)
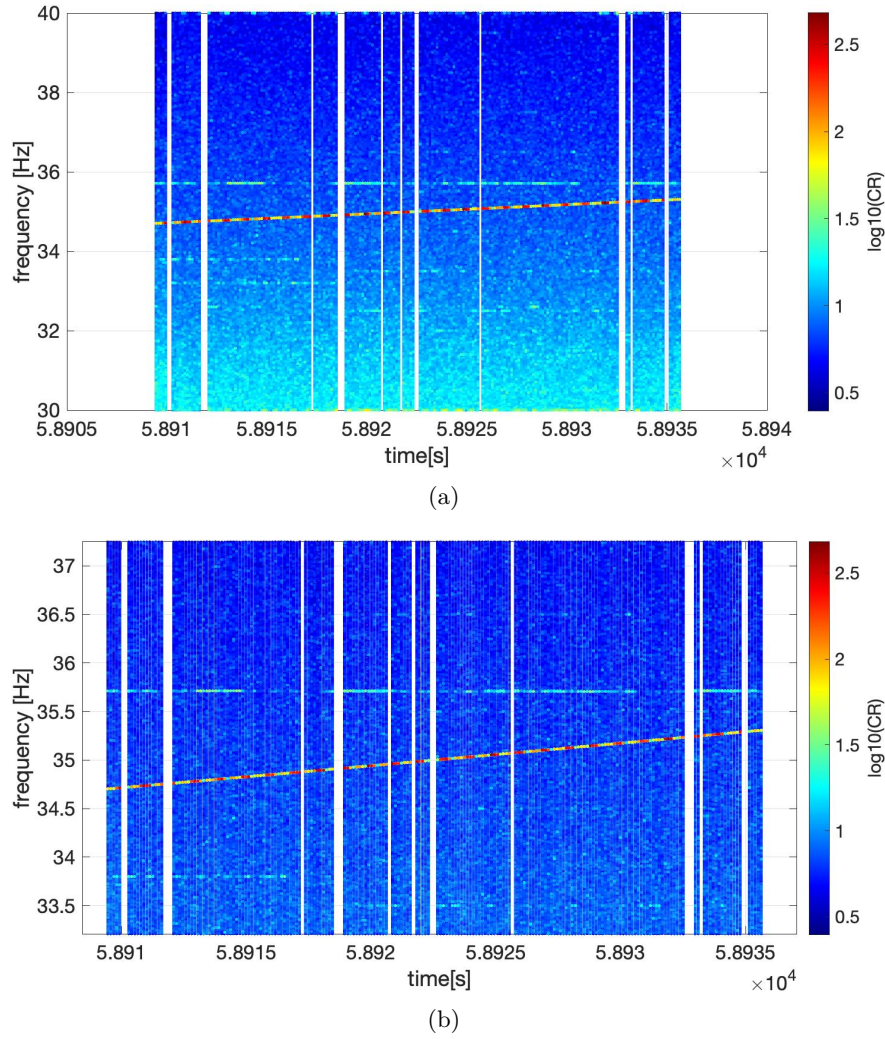
Figure 4.14. *Upper*: Peakmap created with a $T_{FFT} = 20750$ s of a signal after the injection of a signal with: $f_0 = 34.7$ Hz and $M_c = 2.5119 \cdot 10^{-4} M_\odot$. *Bottom*: a zoom of the peakmap on top.

In these peakmaps one can see edge effects, that can appear at multiples of 10 Hz, due to the presence of instrumental spectral lines, and sometimes due to artefacts produced by the construction of the BSD files, which may appear at integer multiples of 10 Hz. As can be seen from the graph in Fig.(4.14), the signal at $f_0 = 34.7$ Hz and $M_c = 2.5119 \cdot 10^{-4} M_\odot$ is most affected by the effect of noise. Indeed, the sensitivity of the Advanced LIGO detector is limited by fundamental noises (mainly seismic noise at low frequency, thermal noise of the mirrors at intermediate frequency, laser shot noise at high frequency) and by many "technical" noises, which appear in the form of time domain glitches and spectral disturbances in the frequency domain.

At this point, we can then correct the signal phase evolution in the time domain using heterodyne. Heterodyne correction is applied to *each* point of the grid. In

an ideal situation, this correction could lead to the signal remaining at a single frequency for its entire duration in the peakmap, as shown before. In practice, it will not be perfect due to the mismatch among the true signal parameters and the values corresponding to the grid points.

Figs. (4.15) and (4.16) show the peakmaps after applying the heterodyne correction for a given grid point in the parameter space. The signal track shows a residual spin-up much smaller than before the coarse correction.
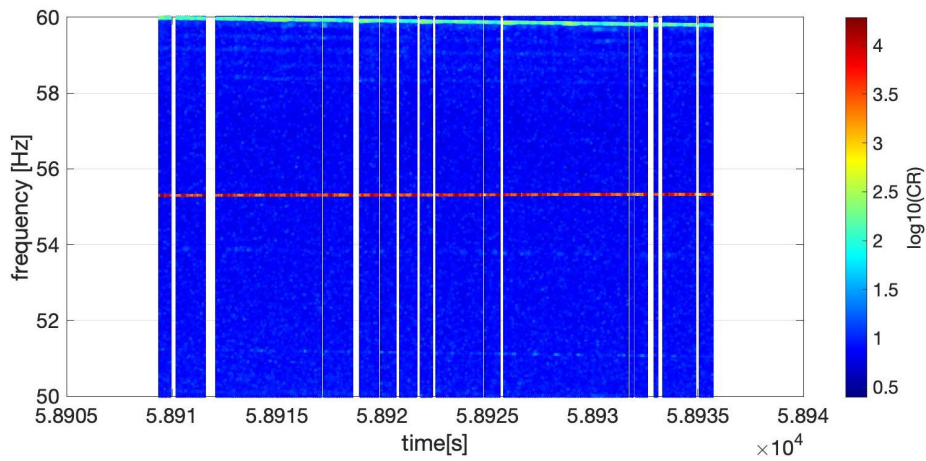
(a)
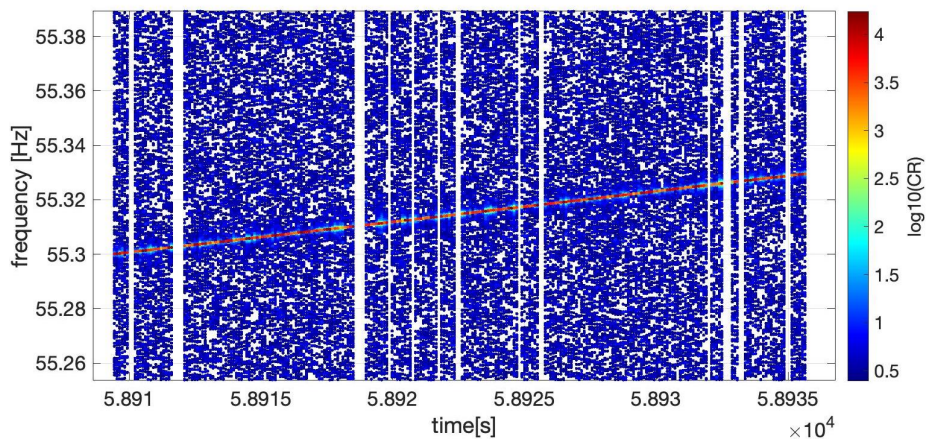
(b)

Figure 4.15. *Upper*: Peakmap of the injected signal after heterodyne correction. *Bottom*: a zoom of the peakmap on top around the frequency of the injection; After the coarse correction the signal will still be affected by a residual frequency variation, due to the non perfect spin-up correction.

(a)

(b)
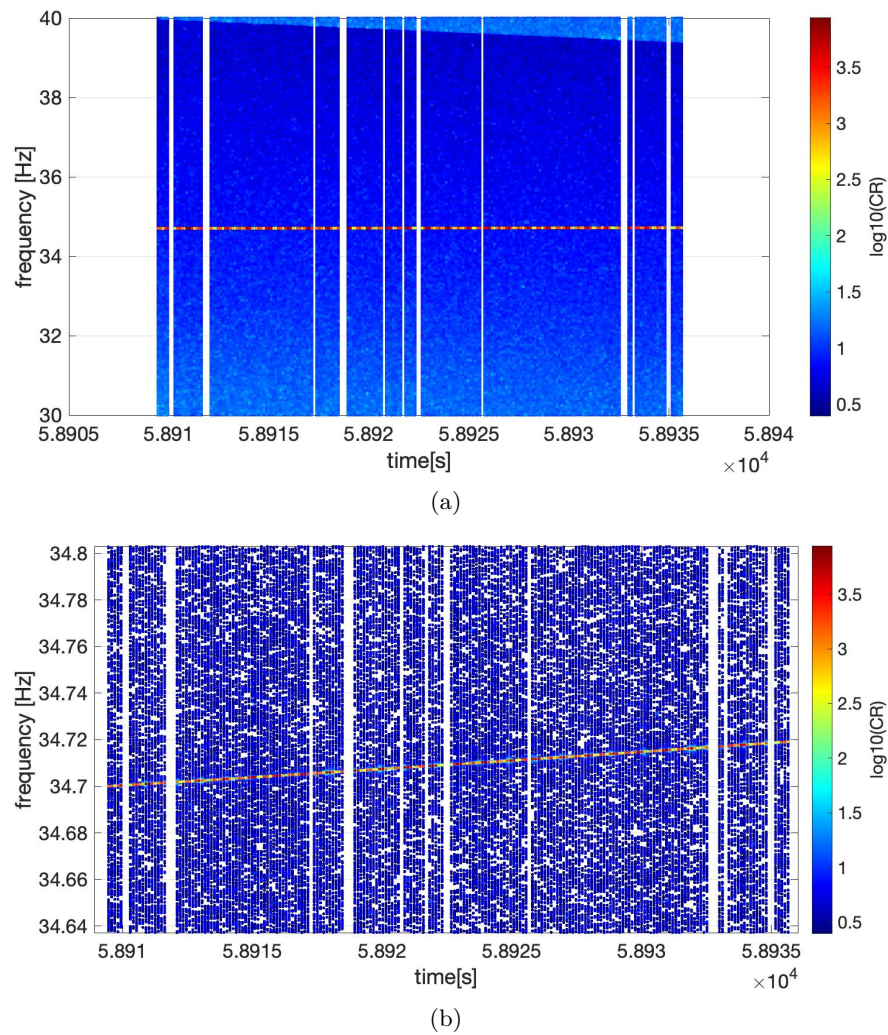
Figure 4.16. *Upper*: Peakmap of the injected signal after heterodyne correction. *Bottom*: a zoom of the peakmap on top.

Only after implementation of the refined correction the signal will be perfectly monochromatic. The peakmaps expected after the refined correction is shown in Fig.(4.17) ans Fig.(4.18).

(a)

(b)
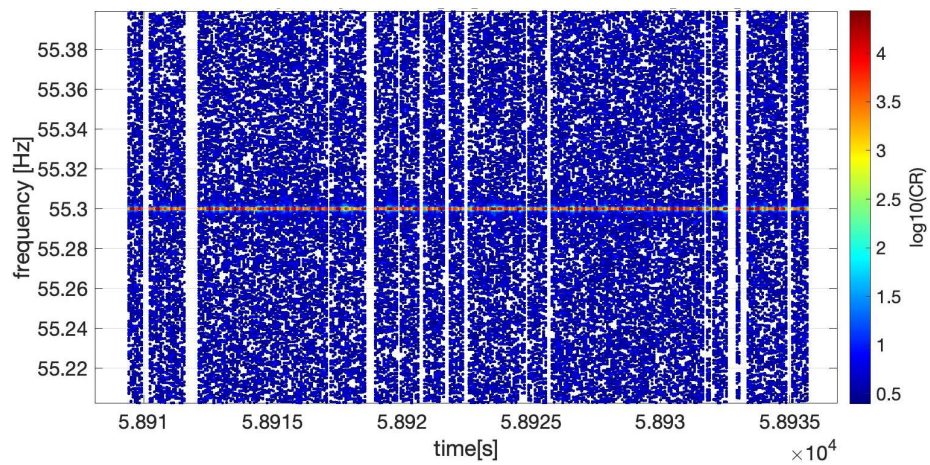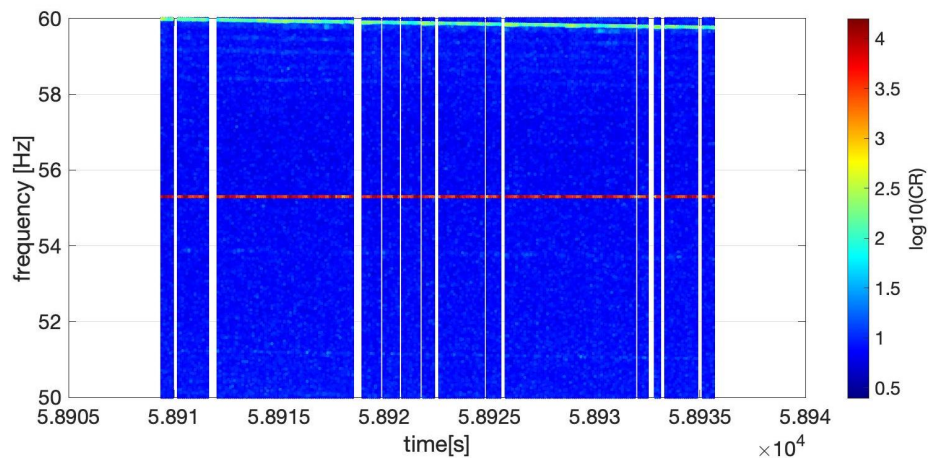
Figure 4.17. *Upper*: Peakmap after refined correction. *Bottom*: zoom of the peakmap on top around the frequency of the injection. After the refined correction, we expect the signal to be perfectly correct and that the residuals are removed.
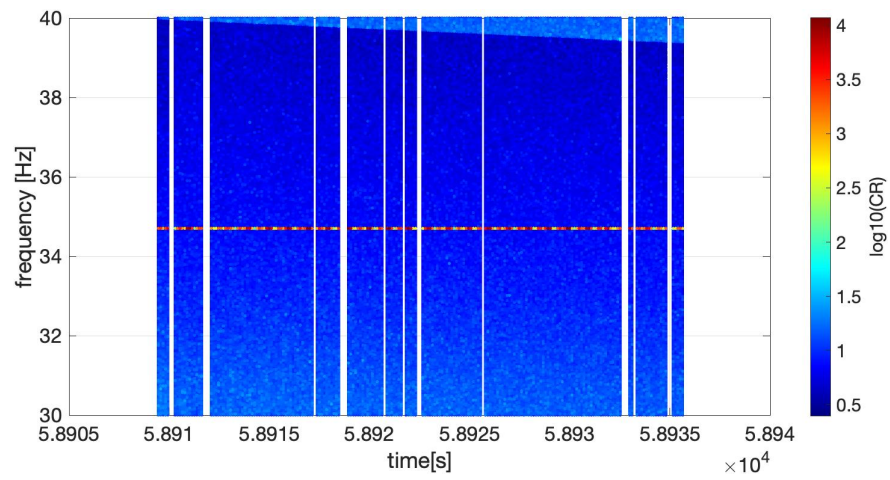
(a) .
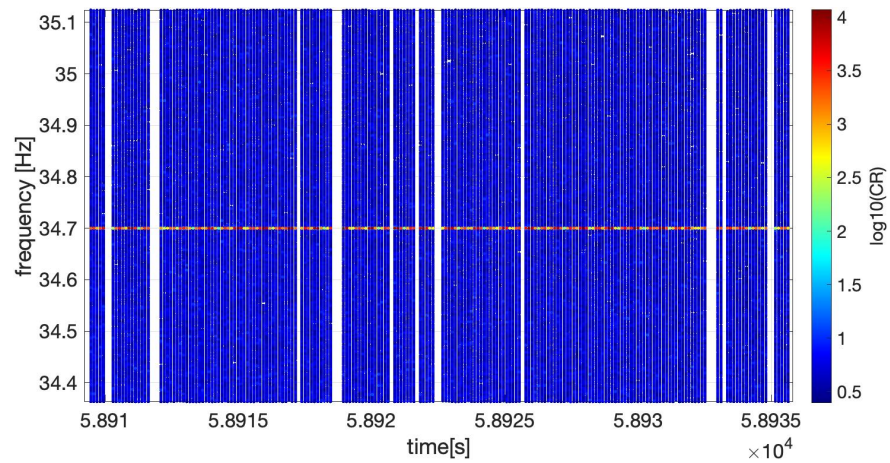
(b) .

Figure 4.18. *Upper*: Peakmap after refined correction. *Bottom*: zoom of the peakmap on top around the frequency of the injection.

The corrected peakmaps are then projected onto the frequency axis (Fig. (4.19)) and.(4.20). If the signal is strong enough, as in this case, it will produce a significant peak on the projection and will be selected for the follow-up stage.
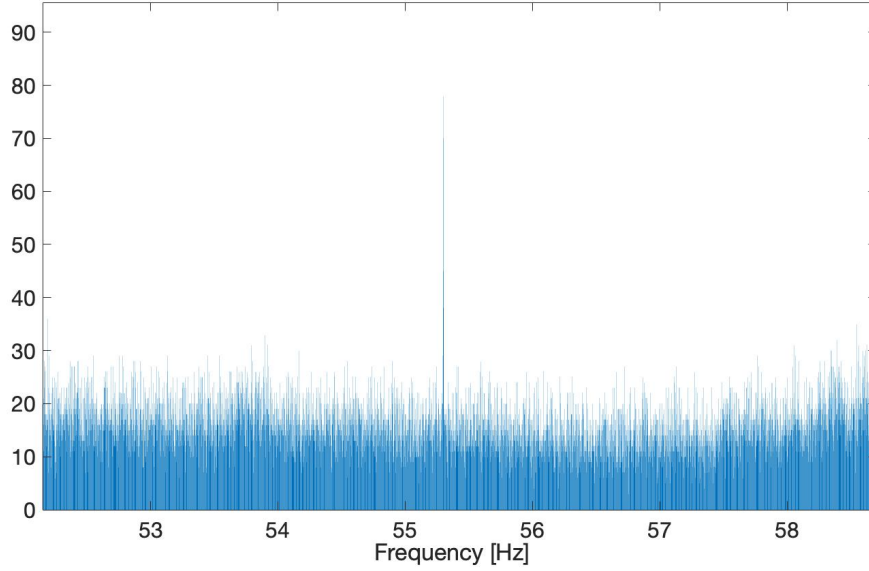
Figure 4.19. The plot represents the number of peaks at a frequency vs the frequency [Hz].The peak corresponds to the injected signal with $f_0 = 55.3$ Hz and $M_c = 5.0119 \cdot 10^{-5} M_\odot$.
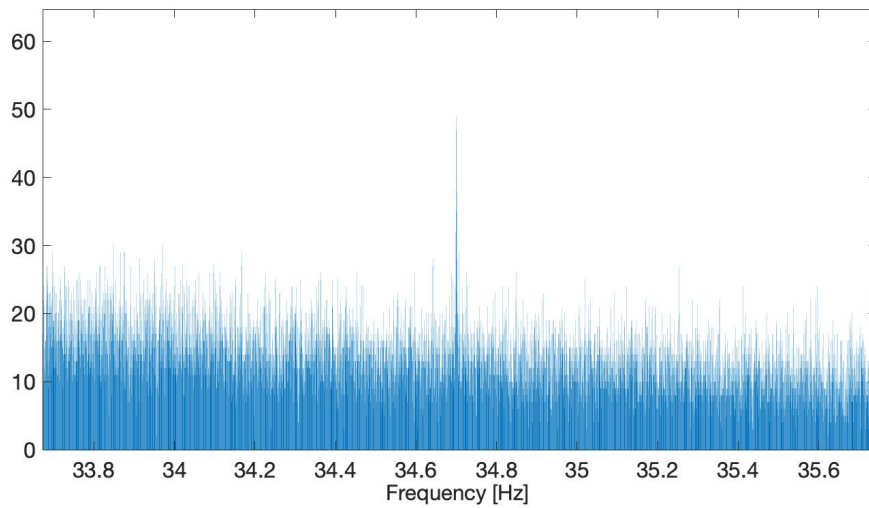
Figure 4.20. The plot represents the number of peaks at a frequency vs the frequency [Hz]. The peak corresponds to the injected signal with $f_0 = 34.7$ Hz and $M_c = 2.5119 \cdot 10^{-4} M_\odot$.

4.7 Sensitivity Estimation

Assuming the signal frequency variations have been properly corrected, as described in previous sections, the sensitivity of a semi-coherent search is related to the observation time, the T_{FFT}, and the power spectral density noise of the detector in the following way:

$$S \propto \frac{h(f)}{\sqrt{S_n(f)}} T_{obs}^{1/4} T_{FFT}^{1/4} \qquad (4.16)$$

The analytical expression for theoretical sensitivity has been found in [37] for signals with strong spin-down, like those emitted by newborn magnetars. In this thesis, we follow the same procedure, extending it to the case of GWs from PBHs in the inspiral phase, when the signal has a strong spin-up and amplitude varies with frequency as $f^{2/3}$. Adapting [37] to our case, we write:

$$h(t_i) = \mathcal{A}f(t_i)^{2/3} = \mathcal{A}\mathcal{F}_i \qquad (4.17)$$

where $\mathcal{F}_i = f(t_i)^{2/3}$, and

$$\mathcal{A} = \frac{4}{d} \left(\frac{GM_c}{c^2} \right)^{5/3} \left(\frac{\pi}{c} \right)^{2/3} \qquad (4.18)$$

The minimum detectable amplitude $\mathcal{A}_{min}$ is given by [37]

$$\mathcal{A}_{min} = \frac{4.02}{N^{1/4}\theta_{thr}^{1/2}} \sqrt{\frac{N}{T_{FFT}}} \left(\sum_i \frac{\mathcal{F}_i^2}{S_n(f_i)} \right)^{-1/2} \times \left(\frac{p_0(1-p_0)}{p_1^2} \right)^{1/4} \sqrt{CR_{thr} - \sqrt{2}erfc^{-1}(2\Gamma)} \qquad (4.19)$$

where the sum is extended to all the data segments of duration T_{FFT}, θ_{thr} is the threshold for the peak selection, p_0 is the probability of selection a peak above the threshold θ_{thr}, $p_1 = e^{-\theta_{thr}} - 2e^{-2\theta_{thr}} + e^{-3\theta_{thr}}$, CR_{thr} is the threshold on the critical ratio used to select outliers and Γ is the chosen confidence level.

It follows from equation (4.19) that the minimum detectable strain amplitude for a given confidence level is a function of the frequency and detector spectral density noise $S_n(f)$; the parameters N, θ_{thr}, CR_{thr}, T_{FFT}, and consequently p_0, p_1 which are functions of θ_{thr}, are set according to the type of search being conducted.

The minimun detectable strain at a given confidence can be obtained from:

$$h_{0,min} = \mathcal{A}_{min} \cdot frequency^{2/3} \qquad (4.20)$$

using a suitable frequency. Following [37], we use the initial frequency f_0.

From the estimate of the minimum detectable strain, the maximum distance reach d_{max} can be obtained by combining the two equations (4.18) and (4.19) and it has the form [38]

$$
d_{max} = 0.995 \left(\frac{GM_c}{c^2}\right)^{5/3} \left(\frac{\pi}{c}\right)^{2/3} \frac{T_{FFT}}{\sqrt{T_{obs}}} \left(\sum_i \frac{\mathcal{F}_i^2}{S_n(f_i)}\right)^{-1/2} \times
$$
$$
\left(\frac{p_0(1-p_0)}{Np_1^2}\right)^{1/4} \sqrt{\frac{\theta_{thr}}{CR_{thr} - \sqrt{2}erfc^{-1}(2\Gamma)}}
$$
(4.21)

We used the formula (4.21) to estimate maximum distance reached on the (f_0, M_c) plane; the T_{FFT} used is the optimal one, given by (4.13), computed for the considered parameter space. The plot (4.21) shows the maximum distance reached at 95% confidence as a function of GW frequency and source mass.
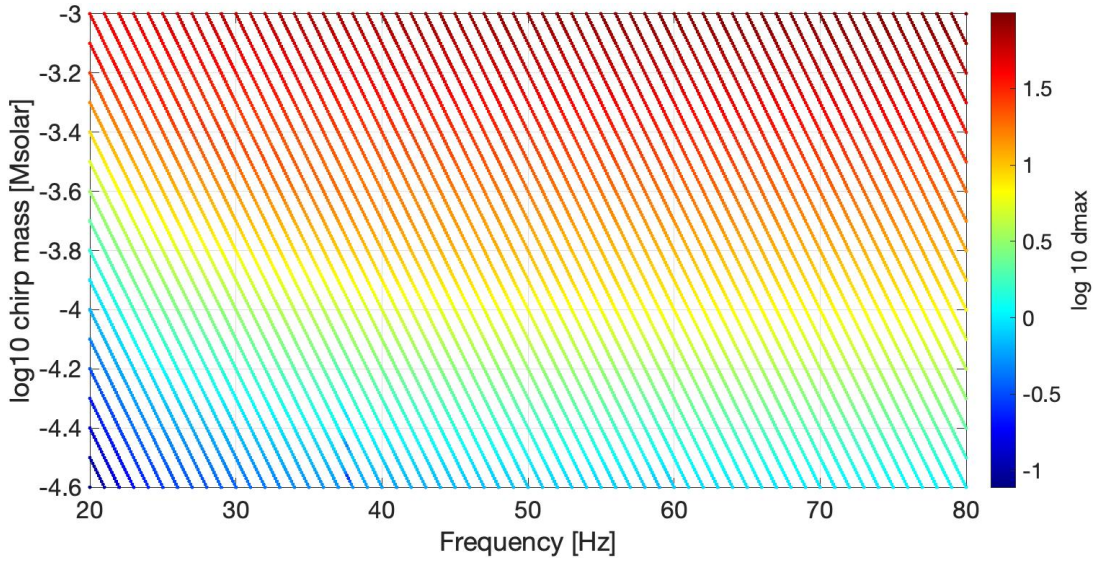
Figure 4.21. Plot shows the maximum distance reached at 95% confidence as a function of parameter space (in kpc). We have used the noise spectral density of Livingstone detector planned for the next run O4, which will start in March 2023. For computational cost reasons, the distance has been computed in a subset of points of the full grid.

First of all, we note that at the portion of parameter space where the optimal T_{FFT} is greater, the distance that can be reached is smaller, as a consequence of the dependence of the signal amplitude on the search parameters, see Eq.(4.19). Secondly, taking that the Milky Away Galactic Center distance as $d = 8$ kpc, the Fig.(4.21) shows an interesting result: the Galactic Center, that is the goal of this thesis, can be reached for a large portion of the considered parameter space (corresponding to yellow area in the graphic and above). Moreover, in the region corresponding to high masses and high frequencies, even greater distances can be reached than the galactic centre. Overall, the distance reached ranges from $\sim$100 pc for lower masses and smaller initial frequencies to 31 kpc at higher initial frequencies and larger masses. This is the first demonstration ever that GW emission from the inspiral if sub-solar mass PBHs located in the galactic center is potentially detectable.

4.8   Computational cost

To achieve greater sensitivity, good and fast data processing is required, as we are generally limited by the available computational power. At a fixed computational cost, we can make two choices: aim for higher sensitivity by exploring a smaller parameter space, or to investigate a larger parameter space but lose in terms of sensitivity.

For a direct search on 1 year of data, with the choices made in this work, we estimate that the heterodyne correction takes about 1 minute. In addition, for each grid point we have to perform: peak map construction, refined correction and projection. For all these operations, we estimate a total time of 3 minutes per detector for one year of data analysis. This results in approximately $3 \times 10^5 \, core \; hours$ *per detector*. The use of a finer grid in parameter space would increase sensitivity at the price of a higher computational load.

4.9   Sky resolution

The choice of the data segment duration, T_{FFT}, has an impact on the sky resolution. Our work is focused on the search of PBH inspirals located in the galactic center region, so we want to understand how the galactic center extension compares to the sky resolution of the search, in order to establish if just one or more sky directions must be taken into account. A dense stellar environment, which could also host PBH, exists in a region of few parsecs around the supermassive black hole Sgr A* [44].
As explained in [12], the sky resolution in ecliptic coordinates (λ, β) is such that two neighbouring sources with the same emission frequency f_0 can be distinguished if the different Doppler correction between the two positions produces a frequency difference greater than the frequency bin: $\Delta f > \delta f = 1/T_{FFT}$. The size of a sky cell will then be determined by the two equations [40]

$$\delta \lambda = \frac{1}{N_D cos\beta} \tag{4.22}$$

$$\delta \beta = \frac{1}{N_D sin\beta} \tag{4.23}$$

where the longitude resolution is $\delta\lambda$, the latitude resolution is $\delta\beta$ and N_D is number of frequency bins in the Doppler band, given by

$$N_D(f_0) \sim 10^{-4} f_0 T_{FFT} \tag{4.24}$$

Eqs. (4.22) and (4.23) determines the angular resolutions along the longitude and the latitude. In practice, Eq. (4.23) provides the step to construct the grid in β, computed starting from the ecliptic north pole and moving downwards to avoid divergence at $\beta = 0$.

For each chirp mass and frequency in the parameter space, we first calculate N_D based on optimal T_{FFT}, and then we compute the values of $\delta\lambda$ and $\delta\beta$ for

the sky grid point nearest to the ecliptic coordinates of the Galactic Center:
$(\lambda_{GC}, \beta_{GC}) = (266.8517, -5.6077^o)$.

In order to give an estimation of the sky patch dimension in degrees, we evaluate
the quantity $d_{sky} = \sqrt{\delta\lambda \cdot \delta\beta}$ for each value of the chirp mass and frequency in the
parameter space (Fig. (4.22)). As expected, the behaviour of T_{FFT} is also reflected
in d_{sky}: for larger T_{FFT}, d_{sky} takes on smaller values and vice-versa. To compare
this sky resolution with the extent of the GC, we very conservatively suppose to
be interested in a spot around Sgr A* of 100×100 pc. The corresponding angular
extent is of the order of $\Delta = 100/8000 = 0.01$ rad ~ 0.57 deg. Observing Fig. (4.22),
we thus see that the sky centre region is completely contained within a single sky
cell for most of the parameter space. Only for smaller initial masses and frequencies
does this not happen and several additional Doppler corrections would be required.
But, on the other hand, as discussed in the previous section, for this portion of the
parameter space the attainable distance is less than that of the Galactic centre and
is therefore less relevant in the context of the present work, whose aim is to reach at
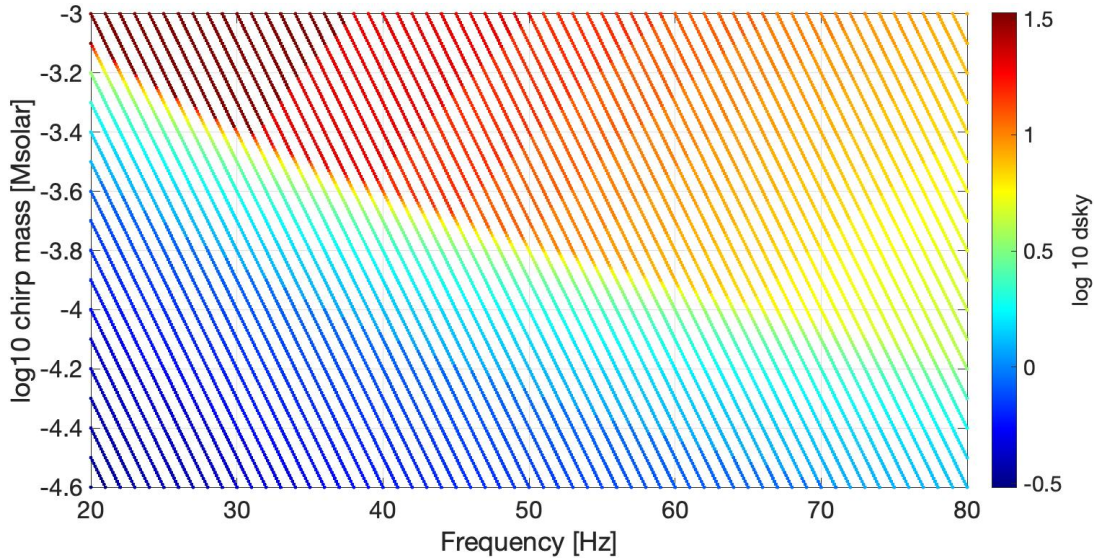least the galactic center.

Figure 4.22. The figure shows the values assumed by d_{sky} depending on chirp mass and
frequency. For computational cost reasons, the distance has been computed in a subset
of points of the full grid.

Conclusions

In this thesis, I describe a possible data analysis method that can increases the sensitivity of the search for GW from PBH binaries with sub-solar masses, with respect to current methods.

The work is divided into two parts. In the first part, I made some preliminary studies aimed at defining a reduced parameter space that would allow the sensitivity to be increased while preserving the computational cost. In particular, using a phenomenological waveform, I demonstrated the validity of the quadruple approximation to model the inspiral phase of these signals. Furthermore, I studied the SNR to justify the choice of limiting the frequency range. As for the masses, I focused on those not covered by standard LVK searches.

The second part represents the heart of the thesis. I discussed the main data analysis technique used to construct a pipeline, the construction of the grid in parameter space and the calculation of the optimal duration of the data segments for the incoherent analysis step. Subsequently, I showed examples of application of the developed pipeline through injection of simulated signals into real data (run O3). The results show that through the heterodyne procedure we are able to perform an initial coarse correction and that, after implementing a refined correction (left for future work), we will be able to correct the signal perfectly.

As a final step, I provided an estimate of sensitivity. By estimating the minimum detectable strain at a given confidence level, the maximum distance reached was calculated. The results show that the Galactic Centre, which is the goal of this thesis, can be reached for a large portion of the parameter space considered. This is the first demonstration ever that GW emission from the inspiral if sub-solar mass PBHs located in the galactic center is potentially detectable.

Bibliography

[1] A brief review on primordial black holes as dark matter. *Phys. Rev. D*, 106, Jun 2011. doi: `10.1103/PhysRevLett.106.241101`.

[2] B. Abbott and et al. Beating the spin-down limit on gravitational wave emission from the crab pulsar. *The Astrophysical Journal*, 683, 2008. doi: `10.1086/591526`.

[3] B. Abbott and et al. Search for subsolar mass ultracompact binaries in advanced ligo's second observing run. *Phys. Rev. Lett.*, 123, 2019. doi: `10.1103/PhysRevLett.123.161102`.

[4] B. P. Abbott, R. Abbott, T. D. Abbott, M. R. Abernathy, and et al. Observation of gravitational waves from a binary black hole merger. *Phys. Rev. Lett.*, 116:061102, Feb 2016. doi: `10.1103/PhysRevLett.116.061102`.

[5] B. P. Abbott and et. al. Binary black hole mergers in the first advanced ligo observing run. *Phys. Rev. Lett.*, 6, Oct 2016. doi: `10.1103/PhysRevX.6.041015`.

[6] R. Abbott. Search for subsolar-mass binaries in the first half of advanced ligo and virgo's third observing run. *Phys. Rev. Lett.*, 129. doi: `10.1103/PhysRevLett.129.061104`.

[7] R. Abbott and et al. Gwtc-2: Compact binary coalescences observed by ligo and virgo during the first half of the third observing run. *Phys. Rev. X*, 11, Jun 2021. doi: `10.1103/PhysRevX.11.021053`.

[8] R. Abbott and et al. *Physical Rev. D*, 106, Nov 2022. doi: `10.1103/PhysRevD.106.102008`.

[9] R. e. a. Abbott. Search for subsolar-mass binaries in the first half of advanced ligo's and advanced virgo's third observing run. *Phys. Rev. Lett.*, 129, Aug 2022. doi: `10.1103/PhysRevLett.129.061104`.

[10] B. Allen and et al. Findchirp: An algorithm for detection of gravitational waves from inspiraling compact binaries. May 2021. doi: .

[11] J. M. Antelis and C. Moreno. Obtaining gravitational waves from inspiral binary systems using ligo data. *Journal reference: Eur. Phys. J. Plus*, 132, Mar 2017. doi: `arXiv:1610.03567v2`.

[12] P. Astone, A. Colla, S. D'Antonio, S. Frasca, and C. Palomba. Method for all-sky searches of continuous gravitational wave signals using the Frequency-Hough transform. Phys. Rev. D, 90(4):042002, Aug. 2014. doi: `10.1103/PhysRevD.90.042002`.

[13] P. Astone, A. Colla, S. D'Antonio, S. Frasca, C. Palomba, and R. Serafinelli. Method for narrow-band search of continuous gravitational wave signals. *Physical Reviewed D*, 89, Mar 2014. doi: `10.1103/PhysRevD.89.062008`.

[14] P. Astone, S. D'Antonio, S. Frasca, , and C. Palomba. A method for detection of known sources of continuous gravitational wave signals in non- stationary data. *Class. Quantum Grav*, 27, Sep 2010. doi: `10.1088/0264-9381/27/19/194016`.

[15] M. Bassan and F. Ricci. Experimental Gravitation. `https://sites.google.com/a/uniroma1.it/fulvio-ricci/didattica/gravitazione-sperimentale`.

[16] B. Carr and et al. Primordial black hole constraints for extended mass functions. *Phys. Rev. D*, 96, 2017. doi: `10.1103/PhysRevD.96.023514`.

[17] B. Carr and F. Kuhnel. Primordial black holes as dark matter candidates. *Journal of Physics G: Nuclear and Particle Physics*, 5 2022. doi: `0.21468/SSciPostPhysLectNotes.48`.

[18] B. J. Carr. The primordial black hole mass spectrum. *Astrophysical Journal*, 201, Oct 1975. doi: `10.1086/153853`.

[19] B. J. Carr. Constraints on primordial black holes. *Rep. Prog. Phys*, 84, Dec 2021. doi: `10.1088/1361-6633/ac1e31`.

[20] M. W. Choptuik. Universality and scaling in gravitational collapse of a massless scalar field. *Phys. Rev. Lett.*, 70, Jen 1993. doi: `10.1103/PhysRevLett.70.9`.

[21] M. Crawford and D. N. Schramm. Spontaneous generation of density perturbations in the early universe. *Nature*, 298, 1982. doi: `10.1038/298538a0`.

[22] C. Cutler and É. E. Flanagan. Gravitational waves from merging compact binaries: How accurately can one extract the binary's parameters from the inspiral waveform? Phys. Rev. D, 49(6):2658–2697, Mar. 1994. doi: `10.1103/PhysRevD.49.2658`.

[23] V. De Luca, G. Franciolini, P. Pani, and A. Riotto. The evolution of primordial black holes and their final observable spins. *Journal of Cosmology and Astroparticle Physics*, 2020. doi: `10.1088/1475-7516/2020/04/052`.

[24] A. Dolgov and J. Silk. Baryon isocurvature fluctuations at small scales and baryonic dark matter. *Phys. Rev. D*, 47, May 1993. doi: `10.1103/PhysRevD.47.4244`.

[25] A. Einstein. *The Formal Foundation of the General Theory of Relativity.*

[26] V. Ferrari, L. Gualtieri, and P. Pani. *General Relativity and its Applications: Black Holes, Compact Stars and Gravitational Waves.* CRC Press, 1 edition.

[27] J. García-Bellido, J. se Nuno Siles, and E. Ruiz Morales. Bayesian analysis of the spin distribution of ligo/virgo black holes. *Physics of the Dark Universe*, 31. doi: `10.1016/j.dark.2021.100791`.

[28] E. R. Harrison. Fluctuations at the threshold of classical cosmology. *Phys. Rev. D*, 1, 1970. doi: `10.1103/PhysRevD.1.2726`.

[29] S. Hawking. *Gravitationally collapsed objects of very low mass.* 1971.

[30] S. Hawking. Particle creation by black holes. *Commun.Math.Phys*, 46, 1976. doi: `10.1007/BF01608497`.

[31] J. Janquart. Gravitational waves signal analysis: Matched filtering, typical analyses and beyond.

[32] K. Jedamzik. Primordial black hole formation during the qcd epoch. *Phys. Rev. D*, 55, 1997. doi: `10.1103/PhysRevD.55.R5871`.

[33] K. D. Kokkotas. Gravitational Wave Astronomy. *Reviews in Modern Astronomy*, 20:140, Oct. 2008. doi: `10.1002/9783527622993.ch7`.

[34] A. Le Tiec and J. Novak. Theory of Gravitational Waves. In G. Auger and E. Plagnol, editors, *An Overview of gravitational waves: Theory and detection*, volume 457 of *World Scientific*, 2016.

[35] P. Leaci, A. Astone, P Colla, S. D'Antonio, S. Frasca, C. Palomba, O. Piccinni, and M. S. Novel directed search strategy to detect continuous gravitational waves from neutron stars in low- and high-eccentricity binary systems. *Phys. Rev. D*, 95, Jun 2018. doi: `10.1103/PhysRevD.95.122001`.

[36] M. Maggiore. *Gravitational Waves: Theory and Experiments.* Oxford University Press, 1 edition.

[37] A. L. Miller and et. A method to search for long duration gravitational wave transients from isolated neutron stars using the generalized frequency hough. *Phys.Rev.D*, 98, Nov 2018. doi: `10.1103/PhysRevD.98.102004`.

[38] A. L. e. a. Miller. Probing planetary-mass primordial black holes with continuous gravitational waves. *Physics of the Dark Universe*, 32, May 2021. doi: `10.1016/j.dark.2021.100836`.

[39] K. e. a. Mitman. Nonlinearities in black hole ringdowns. Nov 2022. doi: `10.48550/arXiv.2208.07380`.

[40] O. Piccinni, P. Astone, S. D'Antonio, S. Frasca, G. Intini, P. Leaci, A. Mastrogiovanni S Miller, and C. Palomba. Directed search for continuous gravitational-wave signals from the galactic center in the advanced ligo second observing run. *Phys. Rev. D*, 101, May 2020. doi: `10.1103/PhysRevD.101.082004`.

[41] O. J. Piccinni, P. Astone, S. D'Antonio, S. Frasca, G. Intini, P. Leaci, S. Mastro-giovanni, A. Miller, C. Palomba, and A. Singhal. A new data analysis framework for the search of continuous gravitational wave signals. *Classical and Quantum Gravity*, 36(1):015008, Jan. 2019. doi: `10.1088/1361-6382/aaefb5`.

[42] O. J. Piccinni and et al. A new data analysis framework for the search of continuous gravitational wave signals. *Classical and Quantum Gravity*, 36. doi: `0.1088/1361-6382/aaefb5`.

[43] P. Schmidt. Gravitational waves from binary black hole mergers: Modeling and observations. *Frontiers in Astronomy and Space Sciences*, 7, June 2022. doi: `10.3389/fspas.2020.00028`.

[44] R. Schodel and A. Eckart. The structure of the nuclear stellar cluster of the milky way. *J. Phys.: Conf. Ser*, 54. doi: `10.1088/1742-6596/54/1/041`.

[45] P. Villanueva-Domingo, O. Mena, and S. Palomares-Ruiz. Inspiral-merger-ringdown waveforms for black-hole binaries with nonprecessing spins. *Front. Astron. Space Sci*, May 2021. doi: `doi:10.3389/fspas.2021.681084`.

[46] S. Wang, T. Terada, and K. Kohri. Prospective constraints on the primordial black hole abundance from the stochastic gravitational-wave backgrounds produced by coalescing events and curvature perturbations. *Phys. Rev. D*, 101, 2020. doi: `10.48550/arXiv.1903.05924`.

[47] J. M. Weisberg and J. H. Taylor. The Relativistic Binary Pulsar B1913+16: Thirty Years of Observations and Analysis. In F. A. Rasio and I. H. Stairs, editors, *Binary Radio Pulsars*, volume 328 of *Astronomical Society of the Pacific Conference Series*, page 25, July 2005. `https://ui.adsabs.harvard.edu/abs/2005ASPC..328...25W`.

[48] J. Yokoyama. Cosmological constraints on primordial black holes produced in the near-critical gravitational collapse. *Phys. Rev. D*, 1998. doi: `10.1103/PhysRevD.58.107502`.

[49] Y. B. Zel'dovich and I. D. Novikov. *The Hypothesis of Cores Retarded during Expansion and the Hot Cosmological Model*. 1966.